Corrosion Science 240 (2024) 112328

Contents lists available at ScienceDirect

Corrosion Science

journal homepage: www.elsevier.com/locate/corsci

The effect of molecular structure of imidazole-based compounds on corrosion inhibition of Cu, Zn, and Cu-Zn alloys

Ingrid Milošev [a,*,1], Peyman Taheri [b], Barbara Kapun [a], Dževad K. Kozlica [a], Arjan Mol [b], Anton Kokalj [a,*,2]

[a] Jožef Stefan Institute, Department of Physical and Organic Chemistry, Jamova c. 39, Ljubljana 1000, Slovenia
[b] Delft University of Technology, Department of Materials Science and Engineering, Mekelweg 2, Delft 2628 CD, The Netherlands

ARTICLE INFO

Keywords:
Copper alloys
Corrosion inhibitors
Electrochemical measurements
DFT modelling
FTIR
XPS

ABSTRACT

Three imidazole-based compounds (imidazole, 2-mercaptobenzimidazole, and 2-mercapto-1-methylbenzimidazole) were studied as corrosion inhibitors of Cu, Zn, and a family of Cu-*x*Zn brass alloys (x = 10−40 wt%) in 3 wt% NaCl solution. The composition of inhibitor layers on the surface was studied using X-ray photoelectron and infrared spectroscopies. The molecular adsorption modes on Cu and Zn were modelled using density-functional theory (DFT) calculations. Mercapto-based inhibitors act as efficient inhibitors on all materials studied due to the formation of inhibitor layer through bonding with nitrogen and sulphur atoms. In contrast, imidazole is a moderate inhibitor for Zn, while it is much less efficient for Cu.

1. Introduction

The ability to design the configuration of an organic molecule, including its skeleton structure and additional functional group(s), to optimise the corrosion inhibition properties of a particular metallic material in a given environment is the ultimate goal of corrosion inhibitor research. Traditionally, this process was based on empirical procedures, including a large number of experiments screening various types of organic compounds. Even if such screening is systematic, it is slow and probably only partially successful. Moreover, even a small change in molecular configuration or substrate composition may significantly affect inhibition efficiency. Contemporary studies are focused on linking molecular characteristics to corrosion efficiency; these include experimental high-throughput methods of testing a large number of potential molecular compounds as inhibitors [1–3] and various computational approaches [4,5], ranging from explicit modelling of inhibitor–surface interactions [6], machine-learning screening models [7], to multi-scale modelling utilising the integrated computational materials engineering (ICME) paradigm [8].

Among the most efficient inhibitors for copper are triazole- and imidazole-based inhibitors [9–12]. The research focus of our experimental and computational modelling studies in the last decade was on benzotriazole (BTAH), benzimidazole (BimH), and their derivatives. Among corrosion inhibitors for copper, BTAH has been by far the most studied compound [10−12,18]. It has been known since 1947 as an outstanding corrosion inhibitor for copper and its alloys [12]. BTAH, with the chemical formula $C_6H_5N_3$, is a heterocyclic compound containing a benzene ring and an azole ring with three nitrogen atoms. It has a strong ability to form N−Cu chemical bonds in deprotonated form [13]. In NaCl solution containing more than 0.05 mM BTAH, a barrier Cu(I)-BTA network is formed, which causes the reduction of current density in both cathodic and, especially, anodic regions [13,14]. DFT modelling revealed that BTAH shows a strong affinity to form intermolecular organometallic aggregates, which seem crucial for outstanding corrosion inhibition due to the formation of compact barrier film [6,13,14]. Derivatives of BTAH and other triazoles, such as amino derivatives of 1,2,4-triazole were also considered [15], among which 3-amino-1,2,4-triazole was shown to be the most effective inhibitor, but still much less than BTAH itself [13]. Additional benzene ring added to BTAH to form naphthotriazole increases corrosion efficiency, but due to high price, naphthotriazole is not used as a corrosion inhibitor [16,17].

In addition to triazoles, another important group of inhibitors for copper are imidazole derivatives [18]. These compounds were investigated in our previous works with emphasis on their usability as

* Corresponding authors.
E-mail addresses: ingrid.milosev@ijs.si (I. Milošev), tone.kokalj@ijs.si (A. Kokalj).
[1] https://www.ijs.si/ijsw/K3-en/Milosev
[2] https://www.ijs.si/ijsw/K3-en/Kokalj

https://doi.org/10.1016/j.corsci.2024.112328
Received 25 April 2024; Received in revised form 23 June 2024; Accepted 26 July 2024
Available online 30 July 2024

corrosion inhibitors using electrochemical and surface analytical techniques [19–23], whereas their adsorption modes on metal surfaces were characterised by DFT calculations [20,22,24]. To shed light on how various functional groups affect the properties of imidazole, the role of mercapto, benzene, and methyl groups on imidazole ring was studied on copper [19,20,24] and iron [25] at 1 mM concentration in 3 wt% NaCl. Benzimidazole is superior to imidazole; adding the mercapto group increases its efficiency even more. 2-mercaptobenzimidazole (MBI), with chemical formula $C_7H_6N_2S$, exists in two tautomer forms, the thione and the thiol (Fig. 1). The thermodynamically preferable tautomer form of the molecule is thione, which has exocyclic C═S and two endocyclic C−N bonds, whereas thiol has endocyclic C═N and C−N bonds and an exocyclic C−SH bond. Comparatively, the thiol form contains both C−N−H (pyrrole) and C═N−C (pyridine) nitrogen atoms, whereas thione contains only the pyrrole type. Deprotonated molecules bind considerably stronger than neutral molecules; dissociation is particularly facile for the thiol tautomer, which involves the S−H bond cleavage [24]. For thione, the dissociation proceeds via the N−H bond breaking, resulting in the thiolate structure analogous to the one originating from the S−H cleaved thiol [24]. Eventually, the molecule is bonded via N−Cu and S−Cu bonds to the substrate. It is also noteworthy that mercapto derivatives show a low tendency to form soluble cupric complexes [24], contributing to their efficiency. In contrast to the mercapto group, the role of the methyl group is still under debate: for 2-mercapto-1-methylimidazole, its efficiency depends on the concentration and the substrate: it is efficient for inhibiting corrosion of iron at all concentrations [25], but for copper, it is efficient only at low concentrations [19]. This finding confirms that the inhibition effect of a given inhibitor strongly depends on the substrate and that the efficiency of the inhibitor cannot be predicted *per se* without considering the substrate [4,26].

The surface-analytical characterisation of MBI by X-ray photoelectron spectroscopy (XPS) was carried out by Chadwick and Hashemi already in 1979 [27] and its good anticorrosion properties were reported by Xue et al. in 1991 [28]. Since then, several comprehensive studies on MBI have been reported on copper, emphasising the complex structure between the inhibitor and cuprous species at the surface [29–32]. It was reported that MBI is also an efficient corrosion inhibitor for aluminium alloys [2]. Recently, the structure of MBI deposited on clean and pre-oxidised Cu(111) was investigated by sophisticated surface analytical tools [33]. A multilayer of MBI can block the initial stages of oxidation of copper under low oxygen pressures at room temperature, and the molecular layer is stable up to 500 °C [33].

In the present work, we continue our previous studies on imidazole-based inhibitors of copper and focus on three organic compounds—imidazole (Imd), 2-mercaptobenzimidazole (MBI), and 2-mercapto-1-methylbenzimidazole (MMBI)—as corrosion inhibitors for copper, zinc, and copper-zinc alloys (brasses, Cu-*x*Zn, where *x* is the weight % of Zn). It was previously reported that BTAH is an efficient inhibitor for brasses with Zn concentration ranging from 10 and 40 wt%, particularly for Cu-10Zn [34], but the utility of mercaptobenzimidazoles is less explored. Therefore, this work aims to compare the efficiency of Imd, MBI, and MMBI compounds on Cu, Cu-*x*Zn alloys, and Zn in NaCl solution and to elucidate the mechanism of inhibition using electrochemical linear and potentiodynamic polarisation measurements, X-ray photoelectron and infrared spectroscopies, and DFT modelling. All three inhibitors are imidazole-based (Fig. 1). Imidazole is an aromatic, five-membered heterocycle compound classified as diazole, i.e., with two nitrogen atoms. MBI and MMBI have a six-membered heterocyclic benzene ring fused with the imidazole ring. Both can exist in thione and thiol tautomer forms, as explained above. The difference between MBI and MMBI is that MMBI has a methyl group attached to nitrogen instead of hydrogen.

2. Experimental

2.1. Materials

Samples were cut from 2 mm thick foil in the form of discs of 15 mm diameter. Copper (99.95 % purity) and zinc (99.5 % purity) were supplied by Goodfellow Cambridge Ltd, and copper-zinc alloys by Wieland-Werke AG, Ulm, Germany. The Cu-*x*Zn alloys are denoted according to their zinc content, where *x* is zinc content in wt%: Cu-10Zn, Cu-20Zn, Cu-30Zn and Cu-40Zn.

Metal samples were ground using, successively, 1200, 2400 and 4000-grit SiC emery papers (LaboPol-5, Struers, Ballerup, Denmark), cleaned ultrasonically in ethanol for 5 minutes, rinsed with deionised water, and dried in a stream of N_2.

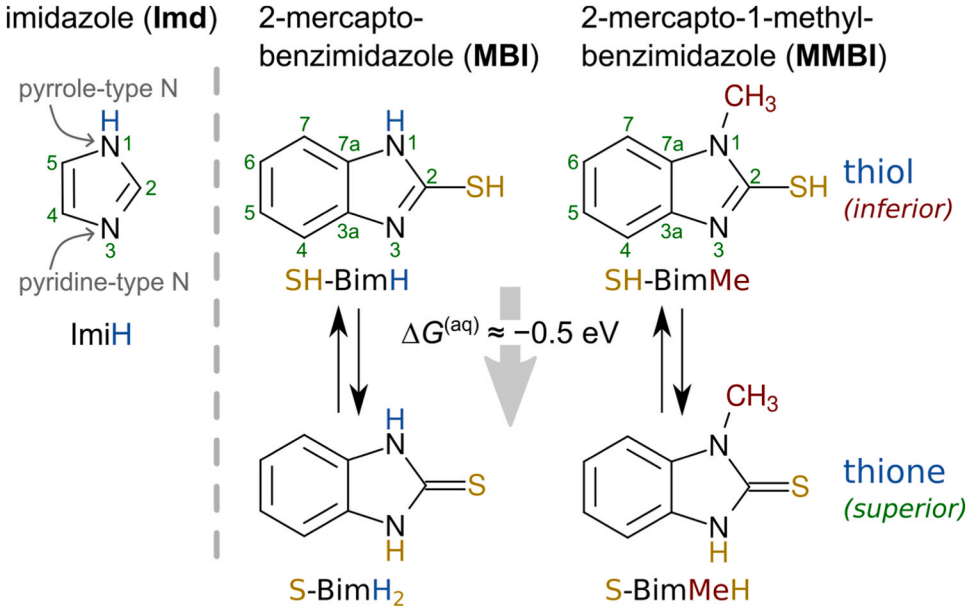

Fig. 1. Molecular skeletal structures of imidazole (Imd), 2-mercaptobenzimidazole (MBI), and 2-mercapto-1-methylbenzimidazole (MMBI). The mercapto molecules display two tautomeric forms, thiol and thione, with the latter being more stable by about 0.5 eV [21]. The labels referring to specific molecular structures are also given (ImiH; SH-BimH and S-BimH_2; SH-BimMe and S-BimMeH).

2.2. Chemicals and solution

Samples were immersed in 3 wt% NaCl aqueous solution with or without the addition of imidazole (Imd), 2-mercaptobenzimidazole (MBI), or 2-mercapto-1-methylbenzimidazole (MMBI) at 1 mM concentration. Structures of these organic compounds are presented in Fig. 1. Compounds were supplied in the form of crystalline powder by Sigma Aldrich (purity for Imd 99.5 %, MBI 98 %, and MMBI 95 %), and NaCl by Carlo Erba (pro analysis) and used without further purification. Solutions were prepared using Mili-Q water (Millipore, Billerica, MA, USA, resistivity 18.2 MΩ cm at 25°C). The pH of the blank NaCl solution is 5.9; the addition of 1 mM organic compound changes the pH to 8.3 for Imd, 5.7 for MBI, and 5.6 for MMBI.

2.3. Molecular labels

The labels Imd, MBI, and MMBI designate the imidazole, 2-mercaptobenzimidazole, and 2-mercapto-1-methylbenzimidazole compounds, respectively. These labels refer to compounds without a specific reference to a particular molecular form. However, as presented in Table 1 and described below, more specific labels are used when referring to a particular molecular form.

The MolH label is used as a generic designation of an intact molecule, whereas a molecule from which an H atom was abstracted is labelled as Mol. Specific labels for imidazole are ImiH for the intact molecule and Imi for the molecule with an H atom abstracted. Furthermore, Imi_{C2} and Imi_{N1} designate the molecule with H abstracted from the C2 and N1 atoms, respectively. The intact MBI and MMBI molecules can exist in two tautomer forms: thiol (R−SH), labelled as SH-BimH and SH-BimMe for MBI and MMBI, respectively, and thione (R=S), labelled as S-$BimH_2$ and S-BimMeH (Fig. 1). The MMBI and MMBI molecules from which an H atom was abstracted are labelled as S-BimH and S-BimMe, respectively.

2.4. Electrochemical measurements

Electrochemical measurements were performed in a three-electrode corrosion cell (Flat Cell, Ametek PAR, K0235, volume 250 mL) at room temperature. The working electrode was the metal substrate with an area of 1.0 cm^2 exposed surface to the corrosive medium. A platinum mesh was used as the counter electrode, and a saturated calomel electrode (SCE) (E = 0.242 V vs. standard hydrogen electrode) was used as the reference electrode. All potentials in the text refer to the SCE scale.

Measurements were performed with potentiostat/galvanostat Autolab PGSTAT 12 (Metrohm Autolab, Nova® software 2.1.3, Utrecht, The Netherlands). For each sample, measurements were performed in at least triplicate. First, time-resolved linear polarisation resistance (LPR) measurements were recorded for 100 h in 3 wt% NaCl with and without added organic compounds, using the range from −10 mV to +10 mV vs. open circuit potential (E_{oc}) at a potential scan rate of 0.1 mV/s; measurements were conducted at 1, 5, 10, 20, 30, 40, 50, 60, 70, 80, 90, and 100 h of immersion. Polarisation resistance (R_p) was determined as the slope of the fitted potential (E) vs. current density (j_{corr}) curve using the Nova 2.1.3 software. Values of R_p are presented as a function of immersion time.

Second, a separate set of experiments was conducted for potentiodynamic (PD) measurements. Upon immersion in an electrolyte (3 wt% NaCl with and without added organic compounds), the sample was allowed to rest at E_{oc}; two separate sets of measurements were conducted at different stabilisation time at E_{oc}, namely of 1 h and 30 h. Following the stabilisation, the polarisation curve was recorded at 1 mV/s potential scan rate, starting at 250 mV below E_{oc} and then increasing the potential in the anodic direction. Corrosion current density (j_{corr}) and corrosion potential (E_{corr}) were determined using Tafel analysis with the Nova® 2.1.3 software. A representative measurement was chosen and presented in plots, whilst in tables, the results are given as mean value ± standard deviation.

2.5. Spectroscopic analysis

Spectroscopic analysis was carried out for samples immersed for 30 h in NaCl solution with and without added organic compound.

The samples were analysed using a Fourier-Transform Infrared Spectrometer (FTIR; Perkin Elmer Spectrum 100, Massachusetts, USA) in the attenuated total reflectance (ATR) mode (a diamond crystal/KRS-5 substrate). The FTIR spectra of the samples were recorded in the range 4000−400 cm^{-1} with a resolution of 4 cm^{-1} and presented as transmittance. As reference samples, Imd, MBI, and MMBI solid powder crystals were analysed.

To examine the interactions between metal surfaces and inhibitors in real time, we employed the ATR-FTIR methodology using the Kretschmann geometry [35]. In this setup, a thin layer of the metal substrate is deposited onto an internal reflection element (IRE). When molecules from a supporting electrolyte interact with this metallic layer, resulting products are analyzed in situ using an infrared beam that passes through the deposited layer and reaches the interface. By measuring the ATR-FTIR peaks, we could correlate them with chemical changes near the metal surface, as the experimental conditions are controlled by the supporting electrolyte.

X-ray photoelectron spectroscopy (XPS) was carried out using a PHI-TFA XPS spectrometer (Physical Electronic Inc.). The vacuum during the XPS analysis was in the range of 10^{-9} mbar. The analysed area was 0.4 mm in diameter, and the analysed depth was about 3–5 nm. X-rays were provided from a monochromatic Al source at a photon energy of 1486.6 eV. Survey and high-energy resolution spectra were recorded. The high-energy resolution spectra were acquired with an energy analyser operating at a resolution of *ca.* 0.6 eV and a pass energy of 29.3 eV. XPS spectra were analysed by Multipak software, version 8.0 (Physical Electronics Inc.). During data processing, the spectra were corrected by setting the C 1 s peak to binding energy (E_b) 284.8 eV, characteristic of C−C/C−H bonds. The accuracy of the binding energies was ± 0.3 eV. Survey XPS spectra were used to deduce the elemental composition of the coating surfaces based on the total intensity of particular element peaks and using values of photoionisation cross sections (C 1 s = 0.857, O 1 s = 2.510, Cu $2p_{3/2}$ = 15.04, Zn $2p_{3/2}$ = 17.026, N 1 s = 1.540, S 2p = 1.544, Cl 2p = 2.09) [36,37].

Table 1
The labels used to designate the imidazole, 2-mercaptobenzimidazole, and 2-mercapto-1-methylbenzimidazole compounds and the respective specific molecular forms.

	imidazole	2-mercaptobenzimidazole	2-mercapto-1-methylbenzimidazole	generic
compound	Imd	MBI	MMBI	/
intact molecule	ImiH	SH-BimH (thiol) S-$BimH_2$ (thione)	SH-BimMe (thiol) S-BimMeH (thione)	MolH
molecule with H abstracted	Imi[a]	S-BimH	S-BimMe	Mol

[a] In addition, the labels Imi_{N1} and Imi_{C2} designate the imidazole molecule with H abstracted from N1 and C2, respectively.

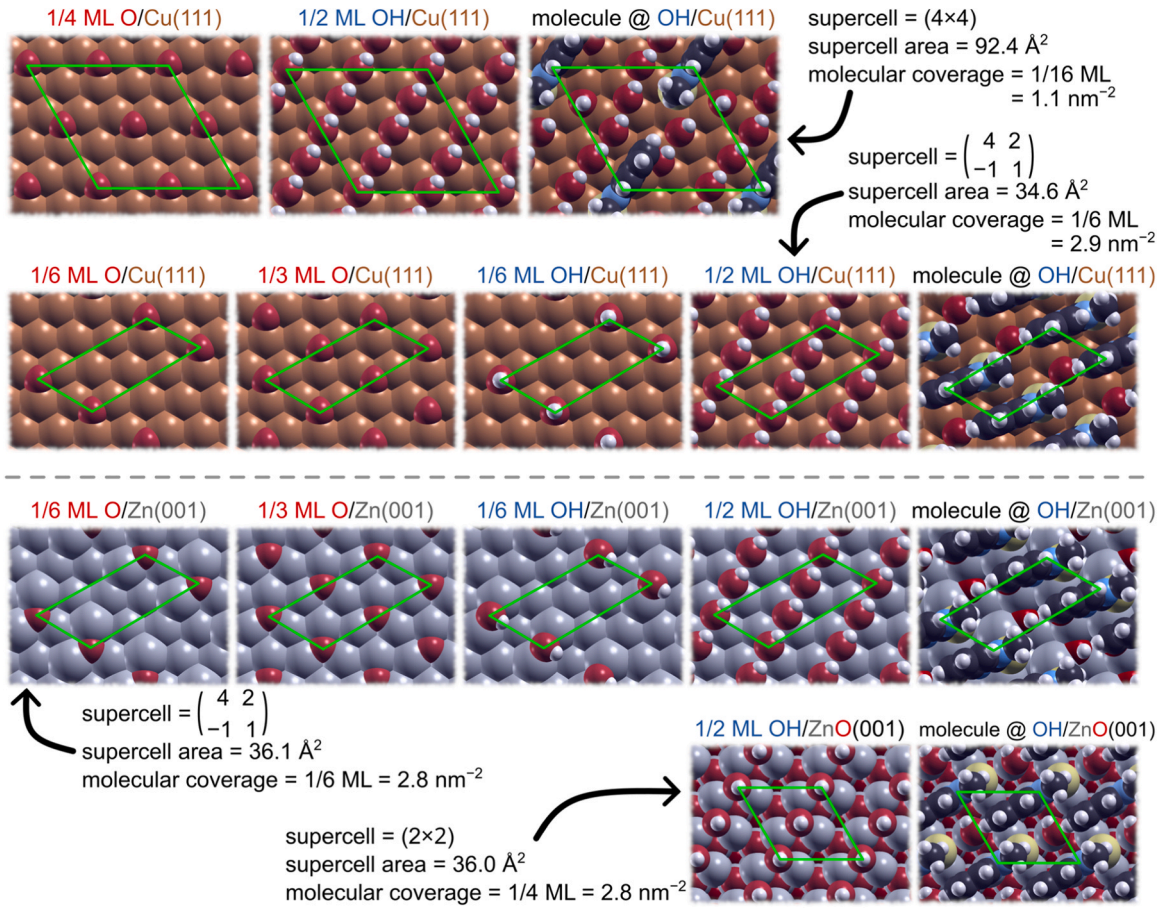

Fig. 2. Top-view snapshots of the utilised Cu and Zn surface models with the supercells indicated by green dashed parallelograms. For each row, the supercell specs and utilised molecular coverages are given. To illustrate molecular coverage, the rightmost snapshot in each row shows a surface model with one molecule per supercell adsorbed. Description of rows from top to bottom: (i) O- and OH-covered Cu(111)–(4×4), (ii) O- and OH-covered Cu(111)–$\begin{pmatrix} 4 & 2 \\ -1 & 1 \end{pmatrix}$, (iii) O- and OH-covered Zn(001)–$\begin{pmatrix} 4 & 2 \\ -1 & 1 \end{pmatrix}$, and (iv) hydroxylated ZnO(001)–(2×2) surface models. For each surface model, the O or OH coverage is stated in ML units.

2.6. DFT calculations

DFT calculations were performed with the PBE+D" method consisting of Perdew–Burke–Ernzerhof (PBE) exchange-correlation functional [38] and a reparametrised D2 empirical dispersion correction of Grimme [39] using the PWscf code from Quantum ESPRESSO distribution [40,41]. The double prime in the PBE+D" label indicates the reparametrised C_6 parameter of Cu to the value of 140 Ry Bohr^{-6} [42] to reduce the molecule−surface overbinding of the original PBE+D2 method [43–45] (the original Grimme's C_6 value for Cu is 375 Ry Bohr^{-6}). Kohn–Sham orbitals were described with a plane wave basis set using a kinetic energy cutoff of 30 Ry, and the cutoff for the electron density was 240 Ry. Core electrons were treated implicitly with the ultrasoft-pseudopotentials [46,47].

Copper and zinc surfaces were described by several different surface models based on O- and OH-covered Cu(111) and Zn(001). In addition, a hydroxylated ZnO(001) was used as a simple model of the oxidised Zn surface. All these slab models correspond to close-packed surfaces because Cu is an fcc and Zn an hcp metal, and ZnO has a wurtzite crystal structure consisting of interpenetrating hcp sublattices of Zn and O ions. These surface models, labeled as O/Cu(111), OH/Cu(111), O/Zn(001), OH/Zn(001), and OH/ZnO(001), are shown in Fig. 2. Two different supercells were used for copper surfaces: a larger (4×4) supercell to model the adsorption of azole molecules at low coverage and a smaller supercell for modelling molecular adsorption at high coverage. Molecular adsorption on zinc surfaces was modelled only at high coverage using the $\begin{pmatrix} 4 & 2 \\ -1 & 1 \end{pmatrix}$ supercell for O- and OH-covered Zn(001) and a (2×2) supercell for hydroxylated ZnO(001). Different coverages of O and OH were used. For the larger (4×4) supercell, the coverage of O and OH was set to 1/4 ML and 1/2 ML, respectively, where the coverage in the ML (monolayer) units is defined as the inverse of the number of surface metal atoms per adsorbate. In contrast, for the smaller $\begin{pmatrix} 4 & 2 \\ -1 & 1 \end{pmatrix}$ supercell, the following coverages were used: 1/6 and 1/3 ML for O, and 1/6 and 1/2 ML for OH. The coverage of OH on the hydroxylated ZnO(001) was 1/2 ML.

The thickness of all slab models was four metal layers (Fig. S1), and the in-plane lattice spacing was set compatible with the respective calculated bulk lattice parameters. The calculated bulk lattice parameters are $a = 3.65$ Å for fcc-Cu, $a = 2.63$ Å and $c = 5.04$ Å for hcp-Zn, and $a = 3.26$ Å and $c = 5.27$ Å for wurtzite-ZnO. For the Cu- and Zn-based slabs, the bottommost metal layer was fixed to the bulk positions, whereas all degrees of freedom were relaxed for hydroxylated ZnO (001). Both sides of the ZnO(001) slab were hydroxylated by 1/2 ML of OH (Fig. S1) to cancel the dipole perpendicular to the slab surface because pristine ZnO(001) is a Tasker type-3 polar surface [48].

The hydroxylated ZnO(001) slab was modelled with the PBE+U+D" scheme using the simplified version of GGA+U method of Cococcioni and de Gironcoli [49] with the U parameter of 7 eV for d-states of Zn ions and 6 eV for p-states of O ions (only the lattice O ions were described with the +U scheme, excluding the O atoms of the OH

groups). Brillouin zone integrations were performed with shifted k-meshes, i.e., 3×3×1 k-mesh for Cu(111)–(4×4), 4×7×1 k-mesh for the $\begin{pmatrix} 4 & 2 \\ -1 & 1 \end{pmatrix}$ supercell of Cu(111) and Zn(001), and 3×3×1 k-mesh for ZnO(001)–(2×2). A Methfessel–Paxton smearing [50] with the smearing parameter of 0.03 Ry was used.

Independently of the surface model, one azole molecule per supercell was adsorbed on the top side of the slab, corresponding to the coverage of 1.1 molecule/nm^2 for the larger Cu(111)–(4×4) supercell and 2.9 molecule/nm^2 for the smaller Cu(111)–$\begin{pmatrix} 4 & 2 \\ -1 & 1 \end{pmatrix}$ supercell. For Zn (001)–$\begin{pmatrix} 4 & 2 \\ -1 & 1 \end{pmatrix}$ and ZnO(001)–(2×2), the molecular coverage corresponds to 2.8 molecule/nm^2 (Fig. 2). Periodic replicas of slabs were separated by at least 18 Å thick implicit solvent region along the surface-normal direction (this value corresponds to the distance between the top of the admolecule and the bottom of the adjacent slab). A quadratic correction to the electrostatic potential along the axis perpendicular to the slab plane was used to correct for electric field artefacts that develop along the direction normal to the slab due to periodic boundary conditions [51].

Calculations were performed in the aqueous phase with the solvent described implicitly using the self-consistent continuum solvation model of Andreussi et al. [52] as implemented in the Environ plugin for Quantum ESPRESSO. Molecular graphics were produced by the XCrySDen [53] graphical package.

2.7. Adsorption modes, energies, and Gibbs energies

We consider both intact (non-dissociative) and dissociative modes of adsorption, the latter proceeding via deprotonation. The non-dissociative adsorption can be written as:

$$\mathrm{MolH} + * \rightarrow \mathrm{MolH}^*, \tag{1}$$

where the label MolH designates an intact molecule, * stands for the free adsorption site, and MolH* for the intact adsorbed molecule. The corresponding adsorption energy is calculated as:

$$E_{\mathrm{ads}} = E_{\mathrm{MolH/slab(aq)}} - E_{\mathrm{MolH(aq)}} - E_{\mathrm{slab(aq)}}, \tag{2}$$

where $E_{\mathrm{MolH/slab(aq)}}$, $E_{\mathrm{MolH(aq)}}$, and $E_{\mathrm{slab(aq)}}$ are total energies of the molecule/slab adsorption system, standalone molecule, and bare slab, respectively; the "(aq)" subscript indicates that all these systems are immersed into an implicit aqueous solvent.

As for dissociative adsorption, it should be noted that the currently utilised surface models contain either O adatoms or OH groups on the surface. On O-covered surfaces, dissociative adsorption can proceed via deprotonation as:

$$\mathrm{MolH} + * + \mathrm{O}^* \rightarrow \mathrm{Mol}^* + \mathrm{OH}^*, \tag{3}$$

where O* stands for the chemisorbed O adatom. The respective dissociative adsorption energy is calculated as:

$$E_{\mathrm{diss\text{-}ads}} = E_{\mathrm{(Mol+OH)/slab(aq)}} - E_{\mathrm{MolH(aq)}} - E_{\mathrm{O/slab(aq)}}, \tag{4}$$

where $E_{\mathrm{(MolH+OH)/slab(aq)}}$ and $E_{\mathrm{O/slab(aq)}}$ stand for total energies of the (Mol+OH)/slab adsorption system and the pristine O-covered slab immersed into the implicit aqueous solvent, respectively. On an OH-covered surface, dissociative adsorption can proceed via a condensation mechanism:

$$\mathrm{MolH} + \mathrm{OH}^* \rightarrow \mathrm{Mol}^* + \mathrm{H_2O}, \tag{5}$$

where OH* stands for the surface OH group. Note that the water molecule is liberated during the adsorption reaction. The respective condensation adsorption energy is calculated as:

$$E_{\mathrm{cond\text{-}ads}} = E_{\mathrm{Mol/slab(aq)}} + E_{\mathrm{H2O(aq)}} - E_{\mathrm{MolH(aq)}} - E_{\mathrm{OH/slab(aq)}}, \tag{6}$$

where $E_{\mathrm{Mol/slab(aq)}}$ and $E_{\mathrm{OH/slab(aq)}}$ are the total energies of the adsorption system and the pristine OH-covered slab immersed into the implicit aqueous solvent, respectively, and $E_{\mathrm{H2O(aq)}}$ is the total energy of a water molecule in the liquid phase, i.e., a self-solvated water molecule.

Gibbs adsorption energies were estimated using the framework described in Ref. [54]. The Gibbs energy at partial pressure (p) and temperature (T) can be written as:

$$G(p,T) = E_0 + G_{\mathrm{corr}}(p,T), \tag{7}$$

where E_0 is the Kohn–Sham total energy, calculated at $T = 0$ K without the zero-point energy (ZPE), as obtained from DFT calculations, and G_{corr} is the difference between the $G(p,T)$ and E_0, which incorporates all terms, such as thermal energy, volume work, and the entropy TS term. The reason for such a decomposition is that calculating Kohn–Sham total energies at 0 K without ZPE is computationally much easier and less CPU intensive than calculating vibrational frequencies needed for calculating ZPE and vibrational contribution to Gibbs energy. For a molecular compound, the $G_{\mathrm{corr}}(p,T)$ term is:

$$G_{\mathrm{corr}}(p,T) = E_{\mathrm{trv}}(T) + pV - TS_{\mathrm{trv}}(p,T), \tag{8}$$

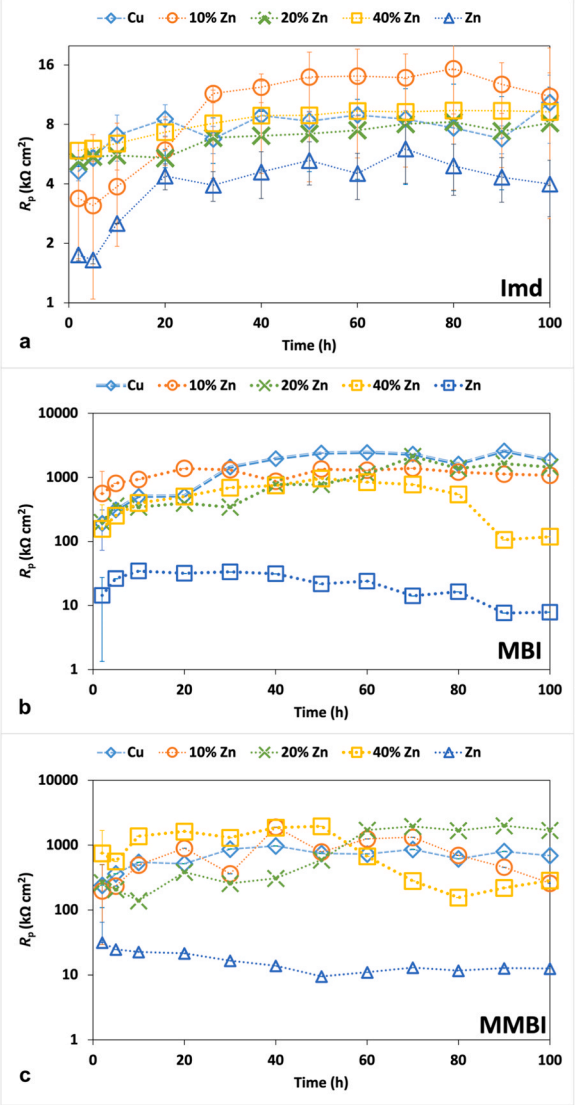

Fig. 3. Polarisation resistance (R_p) as a function of immersion time measured for Cu, Zn, and Cu-xZn alloys in 3 wt% NaCl with 1 mM of (a) Imd, (b) MBI, and (c) MMBI.

where $E_{trv}(T)$ stands for translational + rotational + vibrational thermal energies at temperature T with ZPE included, $S_{trv}(p,T)$ is the translational + rotational + vibrational entropy at p and T, and pV is the volume work. For molecules, the contributions from translational and rotational modes were considered using the ideal-gas approximation and the rigid-rotor model, respectively.[3] For extended systems (surfaces and adsorbates thereon), only the vibrational contribution to thermal energy and entropy is taken into account, and the pV term can be neglected because it is insignificant (solids have about a thousand times smaller volume than gasses at ambient pressure).

To obtain the standard Gibbs energy of a solvated molecular species, one also needs to account for different standard states in the gas phase (partial pressure of 1 atm) and solution (concentration of 1 M). The free energy of solvated species at 1 M concentration can be thus written as:

$$\begin{aligned} G^{1M,(aq)} &= G^{1atm,(aq)} + kT\ln\left(\frac{''1M''}{''1atm''}\right) \\ &= G^{1atm,(aq)} + kT\ln\left(\frac{24.46\ \text{atm}}{1\ \text{atm}}\right) \\ &= G^{1atm,(aq)} + 0.08\ \text{eV} \end{aligned} \tag{9}$$

and

$$G^{1atm,(aq)} = G^{1atm,(g)} + G_{solv}, \tag{10}$$

where $G^{1atm,(g)}$ and $G^{1M,(aq)}$ are the standard gas-phase and aqueous-phase Gibbs energies at the partial pressure of 1 atm and the concentration of 1 M, respectively, and k is the Boltzmann constant (k is used in favour of R because we use eV units). The labels "1M" and "1atm" are symbolic representations of the respective concentrations; at 298.15 K, 1 M corresponds to 24.46 atm, hence "1M"/"1atm" = 24.46. G_{solv} is the Gibbs free energy of solvation. It is worth noting that our calculations are performed in the implicit aqueous solvent with the G_{solv} term already implicitly contained in the E_0 energy of Eq. (7), which is a convenient feature of implicit solvent calculations.

We calculated the Gibbs energies at 1 mM concentration that was used in experiments. Hence:

$$G^{1mM,(aq)} = G^{1M,(aq)} + kT\ln\left(\frac{1\ \text{mM}}{1\ \text{M}}\right) = G^{1M,(aq)} - 0.18\ \text{eV} \tag{11}$$

During condensation adsorption, a water molecule is liberated into the aqueous solvent. The concentration of a liquid water at 298.15 K is 55.34 M. Hence, the free energy of a self-solvated water molecules is:

$$G^{(aq)}_{H_2O} = G^{1M,(aq)} + kT\ln\left(\frac{55.34\ \text{M}}{1\ \text{M}}\right) = G^{1M,(aq)} + 0.10\ \text{eV}. \tag{12}$$

Because calculating vibrational contributions to Gibbs energy is computationally much heavier than calculating other terms, an approximate but useful estimate of the adsorption Gibbs energy can be obtained by neglecting the vibrational contributions for all involved species. According to our experience, the vibrational contributions to adsorption Gibbs energy are usually within ±0.1 eV due to considerable cancellation between reactants and products [55]. The corresponding estimate for the aqueous-phase adsorption Gibbs energy at 1 mM concentration and 298.15 K can thus be written as:

$$\begin{aligned} G^{1mM,(aq)}_{ads} &\approx E_{ads} + G_{roto+transl}(\text{MolH/slab}) - G^{1mM}_{roto+transl}(\text{MolH}) \\ &\quad - G_{roto+transl}(\text{slab}) \\ &\approx E_{ads} - G^{1mM}_{roto+transl}(\text{MolH}), \end{aligned} \tag{13}$$

where, for extended systems, the roto-translational contribution to adsorption Gibbs energy is set to zero because macroscopic objects are immobile, $G_{roto+transl}(\text{MolH/slab}) - G_{roto+transl}(\text{slab}) = 0$. It is worth noting that the dependence of the Gibbs energy on concentration is included in the translational contribution. For dissociative adsorption, the relation between the adsorption Gibbs energy and adsorption energy is analogous to Eq. (13), i.e.:

$$G^{1mM,(aq)}_{diss\text{-}ads} \approx E_{diss\text{-}ads} - G^{1mM}_{roto+transl}(\text{MolH}). \tag{14}$$

In contrast, the relation is more involved for condensation adsorption due to the liberation of a water molecule. Hence, the corresponding adsorption Gibbs energy is:

$$G^{1mM,(aq)}_{cond\text{-}ads} \approx E_{cond\text{-}ads} - G^{1mM}_{roto+transl}(\text{MolH}) + G^{55.34M}_{roto+transl}(H_2O). \tag{15}$$

It is worth reiterating that solvation contribution to the adsorption Gibbs energy is already included in the adsorption energy term (E_{ads}, $E_{ads\text{-}diss}$, or $E_{ads\text{-}cond}$), a convenient feature of implicit solvent calculations. The so-calculated corrections to the adsorption Gibbs energy at 1 mM concentration and 298.15 K are:

$$\begin{aligned} \text{For Imd}: \quad G^{1mM,(aq)}_{ads} &= E_{ads} + 0.80\ \text{eV} \\ G^{1mM,(aq)}_{diss\text{-}ads} &= E_{diss\text{-}ads} + 0.80\ \text{eV} \\ G^{1mM,(aq)}_{cond\text{-}ads} &= E_{cond\text{-}ads} + 0.51\ \text{eV} \end{aligned} \tag{16}$$

$$\begin{aligned} \text{For MBI}: \quad G^{1mM,(aq)}_{ads} &= E_{ads} + 0.91\ \text{eV} \\ G^{1mM,(aq)}_{diss\text{-}ads} &= E_{diss\text{-}ads} + 0.91\ \text{eV} \\ G^{1mM,(aq)}_{cond\text{-}ads} &= E_{cond\text{-}ads} + 0.61\ \text{eV} \end{aligned} \tag{17}$$

$$\begin{aligned} \text{For MMBI}: \quad G^{1mM,(aq)}_{ads} &= E_{ads} + 0.92\ \text{eV} \\ G^{1mM,(aq)}_{diss\text{-}ads} &= E_{diss\text{-}ads} + 0.92\ \text{eV} \\ G^{1mM,(aq)}_{cond\text{-}ads} &= E_{cond\text{-}ads} + 0.62\ \text{eV} \end{aligned} \tag{18}$$

It is worth noting that, for mercapto molecules, adsorption energies and adsorption Gibbs energies are calculated with respect to more stable thione tautomers.

3. Results and discussion

3.1. Polarisation resistance as a function of prolonged immersion time

Upon prolonged immersion in NaCl with and without inhibitor added, the metal surface changes; e.g., it either dissolves, forms a passive oxide or inhibitor-oxide layer, or forms soluble complexes. It is, therefore, prudent to investigate the electrochemical behaviour as a function of time. The dependence of R_p during 100 h immersion seems to be a reliable and non-invasive method for assessing intrinsic inhibitor performance in lab screening studies [21,23]. Diagrams showing R_p vs. immersion time for 100 h for Cu, Cu-10Zn, Cu-20Zn, Cu-40Zn, and Zn in 3 wt% NaCl solution with added inhibitor are presented in Fig. 3 for the three considered compounds. The inhibition action of imidazole is the lowest among the three inhibitors. Depending on the substrate, it reached values between 4 kΩ cm^2 for Zn and 9 kΩ cm^2 for Cu after 100 h immersion. The values for Cu-xZn alloys are closer to that of Cu. In the presence of MBI and MMBI, R_p values increased by two orders of magnitude for Cu and Cu-xZn alloys and one order of magnitude for Zn compared to the values in imidazole-containing NaCl. Please note that the measurements for Cu in blank NaCl after 100 h of immersion gave R_p values of 20 kΩ cm^2 and for Zn less than 1 kΩ cm^2 (results not shown). These long-term measurements thus show that MBI and MMBI are

[3] The ideal-gas translational partition function is $q_{tr} = \left(\frac{mkT}{2\pi\hbar^2}\right)^{\frac{3}{2}} V$, where m is the mass of the molecule, k is the Boltzmann constant, T is the temperature, and V is the volume per ideal-gas particle. For a non-linear molecule, the rotational partition function is $q_{rot} = \frac{1}{\sigma_{rot}} \frac{\sqrt{8\pi(kT)^3 I_A I_B I_C}}{\hbar^3}$, where σ_{rot} is the rotational symmetry number, and I_A, I_B, and I_C are the three eigenvalues of the moment of inertia tensor, which depends on the mass distribution within the molecule. The corresponding entropies are $S_{tr} = k\ (\ln q_{tr} + 5/2)$ and $S_{rot} = k\ (\ln q_{rot} + 3/2)$.

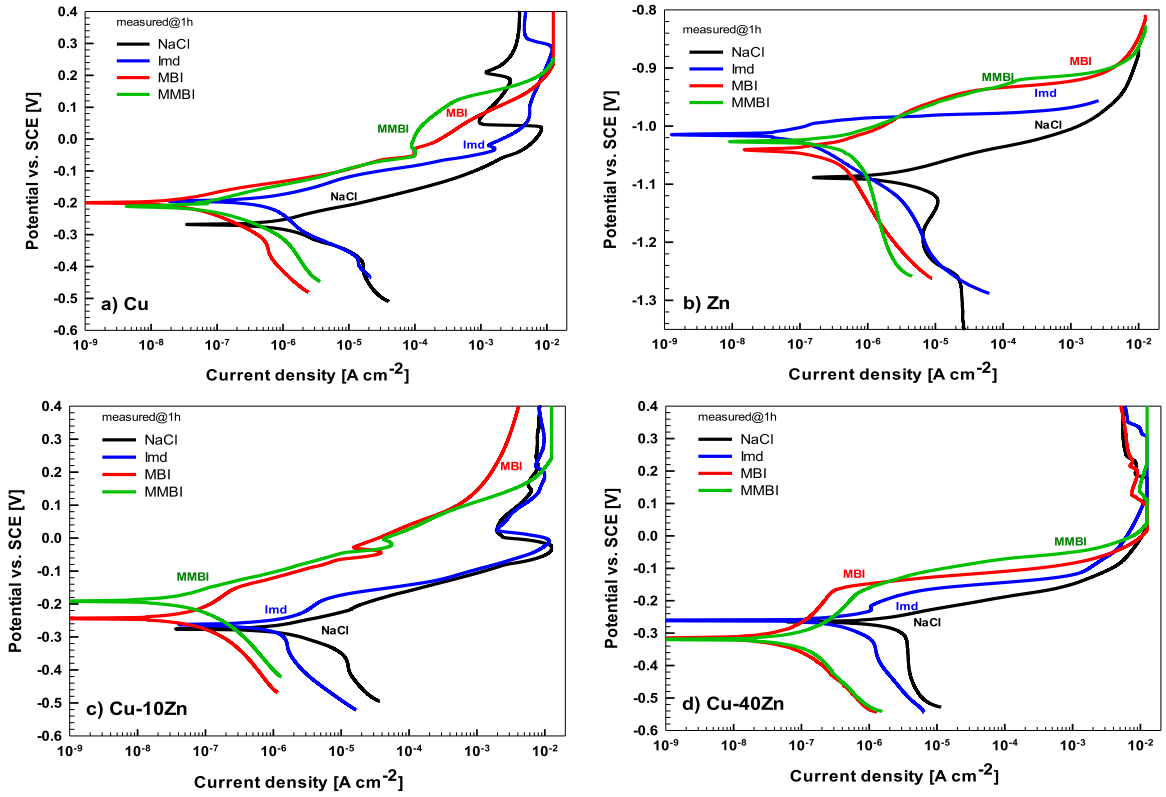

Fig. 4. Potentiodynamic polarisation curves of (a) Cu, (b) Zn, (c) Cu-10Zn, and (d) Cu-40Zn recorded in 3 wt% NaCl with and without added 1 mM Imd, MBI, and MMBI. Stabilisation time at the E_{oc} was 1 h. Electrochemical parameters are given in Table 2.

considerably better inhibitors for Cu than imidazole, which is also valid for Cu-*x*Zn alloys. Moreover, they also seem to protect zinc metal, although to a much lesser extent than other studied materials.

3.2. Potentiodynamic polarisation curves

Potentiodynamic polarisation curves were recorded for Cu, Zn, and the Cu-*x*Zn alloys to study the electrochemical behaviour of these materials in a broad potential range aiming to compare the materials among each other, as well as the inhibition effect of individual inhibitors on the corrosion of each material separately. Polarisation curves are depicted in Fig. 4a–d and electrochemical parameters deduced from the curves (E_{corr}, j_{corr}) are presented in Table 2. Fig. 4a shows the polarisation curves of Cu samples. In the blank NaCl solution, the primary cathodic reaction is the oxygen reduction (reaction 19), while the anodic reaction is the formation of cuprous chloride complexes $CuCl_2^-$, either through the direct reaction of Cu with chloride ions with intermediate formation of CuCl (reactions 20–22), or through a prior dissolution of copper as cuprous ions, subsequently reacting with the chloride ions (reactions 23 and 24) [56,57]:

$$O_2 + 2H_2O + 4e^- \rightarrow 4OH^- \quad (19)$$

$$Cu + 2Cl^- \rightleftharpoons CuCl_2^- + e^- \quad (20)$$

$$Cu + Cl^- \rightleftharpoons CuCl + e^- \quad (21)$$

$$CuCl + Cl^- \rightleftharpoons CuCl_2^- \quad (22)$$

$$Cu \rightleftharpoons Cu^+ + e^- \quad (23)$$

$$Cu^+ + 2Cl^- \rightleftharpoons CuCl_2^- \quad (24)$$

The current density increased exponentially above E_{corr} up to *ca.* 0.05 V, reaching values up to 10 mA cm^{-2}. Then, a current peak was formed, reducing the current density by one order of magnitude. This

Table 2
Electrochemical parameters deduced after 1 h stabilisation at E_{oc} for Cu, Cu-10Zn, Cu-40Zn, and Zn in 3 wt% NaCl with and without 1 mM inhibitor added (Fig. 4). Mean values and standard deviations are given. The current density values at the selected potentials are presented to compare the behaviour in the anodic region (last column).

Solution	Electrochemical parameter		
	E_{corr} [V]	j_{corr} [μA/cm^2]	$j_{E=0\ V}$ [μA/cm^2]
	Cu		
NaCl	−0.244 ± 0.012	1.573 ± 0.169	7889 ± 685
NaCl+Imd	−0.204 ± 0.016	0.508 ± 0.139	3950 ± 2588
NaCl+MBI	−0.204 ± 0.037	0.039 ± 0.013	268 ± 84
NaCl+MMBI	−0.216 ± 0.015	0.045 ± 0.007	150 ± 69
	Cu-10Zn		
NaCl	−0.266 ± 0.021	1.456 ± 0.484	8066 ± 4839
NaCl+Imd	−0.265 ± 0.006	0.389 ± 0.305	1823 ± 506
NaCl+MBI	−0.226 ± 0.010	0.085 ± 0.020	52 ± 40
NaCl+MMBI	−0.183 ± 0.019	0.063 ± 0.041	29 ± 27
	E_{corr} [V]	j_{corr} [μA/cm^2]	$j_{E=-0.2\ V}$ [μA/cm^2]
	Cu-40Zn		
NaCl	−0.260 ± 0.010	2.114 ± 0.313	41 ± 3
NaCl+Imd	−0.274 ± 0.010	0.763 ± 0.264	13 ± 11
NaCl+MBI	−0.335 ± 0.053	0.088 ± 0.030	0.3 ± 0.2
NaCl+MMBI	−0.304 ± 0.035	0.113 ± 0.010	0.6 ± 0.3
	E_{corr} [V]	j_{corr} [μA/cm^2]	$j_{E=-0.95\ V}$ [μA/cm^2]
	Zn		
NaCl	−1.084 ± 0.004	5.21 ± 1.54	6146 ± 851
NaCl+Imd	−1.034 ± 0.047	0.283 ± 0.220	2479 ± 160
NaCl+MBI	−1.014 ± 0.019	0.511 ± 0.275	23 ± 12
NaCl+MMBI	−1.027 ± 0.025	0.380 ± 0.106	18 ± 9

peak is related to the formation of CuCl (reaction 21), covering the surface and subsequently reacting with chloride ions forming $CuCl_2^-$. Further oxidation of copper and cuprous ions occurs in this region, forming cupric ions (reaction 25).

$$CuCl_{2(ads)}^- \rightleftharpoons Cu^{2+} + 2Cl^- + e^- \quad (25)$$

Fig. 4a also shows that adding Imd, MBI, and MMBI shifted the E_{corr} up to 40 mV more positively (Table 2). The effect of Imd on the cathodic current density was insignificant. However, the values were smaller for *ca.* one order of magnitude for the other two inhibitors. The main effect for all three inhibitors occurred in the anodic range, where the increase in current density with potential was much slower than in NaCl only. Additionally, the current density of the anodic peak was established at smaller currents, i.e., from *ca.* 10 mA cm^{-2} in NaCl down to 0.1 mA cm^{-2} with MMBI added. Following the anodic peak, a passive range was established up to *ca.* 0.1 V for MMBI. At more positive potentials, the current density increased abruptly due to the localised breakdown of the passive film at the breakdown potential (E_{break}).

Due to the lower electronegativity of Zn, its E_{corr} in NaCl solution is located at more negative potentials compared to Cu, i.e., at −1.08 V (Fig. 4b). The main cathodic reaction on Zn in aerated NaCl differs from that on Cu. At potentials about 500 mV lower than E_{corr}, hydrogen evolution occurs by reduction of water (reaction 26), and the ZnO film formed during exposure to air is reduced to Zn [58–60]. As the potential becomes more positive, the rate of H_2 evolution decreases. The oxygen reduction occurs through the 4e$^-$ oxygen reduction process (reaction 27). At *ca.* −1.1 V, the oxidation of ZnO occurs by precipitation during cathodic alkanization (reaction 28). This film is not protective due to its porous nature [58,60]. A 4e$^-$ oxygen reduction ceases, and that of the 2e$^-$ process takes place in the vicinity of E_{corr} (reactions 29 and 30):

$$2H_2O + 2e^- \rightarrow H_2 + 2OH^- \quad (26)$$

$$O_2 + 2H_2O + 4e^- \rightarrow 4OH^- \quad (27)$$

$$Zn + 2OH^- \rightarrow ZnO + H_2O + 2e^- \quad (28)$$

$$O_2 + 2H_2O + 2e^- \rightarrow HO_2^- + OH^- \quad (29)$$

$$HO_2^- + H_2O + 2e^- \rightarrow 3OH^- \quad (30)$$

Above $E_{corr} = -1.08$ V, dissolution of zinc begins (reaction 31) [58, 60]. During prolonged immersion, Zn^{2+} ions can react with OH^- to form $Zn(OH)_2$, parts of which can be dehydrated to form ZnO (reaction 32) [60], as also shown by the XPS analysis below. In the presence of chloride ions, the formation of zinc chloride hydroxide can form (reaction 33) [60].

$$Zn \rightarrow Zn^{2+} + 2e^- \quad (31)$$

$$Zn^{2+} + 2OH^- \rightarrow Zn(OH)_2 \rightarrow ZnO + H_2O \quad (32)$$

$$5Zn^{2+} + 8OH^- + 2Cl^- + H_2O \rightarrow Zn_5(OH)_8Cl_2{\cdot}H_2O \quad (33)$$

The addition of Imd, MBI, and MMBI to NaCl strongly influenced the electrochemical response of Zn and shifted the E_{corr} for *ca.* 100 mV more positively. The positive shift was the most pronounced for Imd, as well as the decrease in the j_{corr}. In the anodic branch, the increase in current density with potential was slower with inhibitors added. Comparing the effect of Imd on Cu and Zn, it can be stated that after 1 h at the E_{oc}, Imd is a more efficient inhibitor for Zn corrosion than for Cu since the decrease in j_{corr} was almost 19-fold for Zn and 3-fold for Cu (Table 2).

Polarisation curves of the Cu-*x*Zn alloys in NaCl generally resemble more Cu than Zn, as reported previously [34], but with increasing Zn content, the resemblance to the Zn curve became evident, especially in the cathodic branch. In Fig. 4c and d, the results are presented for Cu-10Zn and Cu-40Zn, whereas results for all four alloys are given in Supplemental information (Fig. S2). With increasing Zn content, the inhibitor action is somewhat reduced but still much improved compared to Zn metal (Fig. S3). Deduced electrochemical parameters for Cu, Cu-*x*Zn, and Zn in NaCl with and without inhibitors added are presented graphically in Fig. S4. Values of j_{corr} decreased the most for MBI an MMBI (Fig. S4a). As for the E_{corr} trend of Cu-*x*Zn, Imd, MBI, and MMBI exhibit the E_{corr} values closer to that of Cu metal than Zn metal with *ca.* 1 V more negative E_{corr} (Fig. S4b). Compared to the blank NaCl solution, the addition of inhibitors induced a positive E_{corr} shift indicating they act like mixed inhibitors with the predominant anodic effect; however, for Cu-*x*Zn alloys with higher Zn content, a negative shift was observed, indicating their significant effect on the cathodic reaction too, as observed in polarisation curves (Fig. 4). Regarding the reduction in j_{corr}, Imd acts as the weakest inhibitor, whilst MBI and MMBI are stronger inhibitors and behave similarly. All considered Cu-*x*Zn alloys benefit strongly from the inhibitor actions.

To elucidate the effect of immersion time on the electrochemical behaviour, we selected to conduct another set of polarisation curves after changing the stabilisation time at E_{oc} from 1 h to 30 h (Fig. 5, S5, and S6, and Table 3). For Cu and Cu-10Zn alloy, the shape of the curves generally remains similar, with j_{corr} somewhat increasing. More significant changes occurred in the anodic region: the current density at the plateau following the peak at *ca.* −0.05 V was reduced, and its extent increased. As a comparative parameter,[4] the current density at 0 V was taken for Cu and Cu-10Zn alloy ($j_{E=0\ V}$); for the Cu-40Zn alloy and Zn, the values at −0.2 V and −0.95 V were taken, respectively ($j_{E=-0.2\ V}$ and $j_{E=-0.95\ V}$); these parameters are presented in Tables 2 and 3. Evidently, the $j_{E=0\ V}$ values were smaller after prolonged immersion of Cu and Cu-10Zn in NaCl containing MBI and, especially, MMBI. For the Cu-40Zn alloy, the $j_{E=-0.2\ V}$ values were smaller for more than one order of magnitude as the immersion time increased from 1 h to 30 h in a solution containing mercapto-based inhibitors. The inhibitive action of imidazole deteriorated with immersion time for all materials investigated. These results confirm much better inhibitive action of MBI and MMBI than that of Imd.

3.3. Spectroscopic analysis of the surfaces

Spectroscopic analyses, including ATR-FTIR and XPS, were performed on samples immersed for 30 h in 3 wt% NaCl with and without (blank) added 1 mM Imd, MBI, and MMBI. Longer immersion time was chosen to form well-developed inhibitor layers. FTIR analysis was conducted on only Cu and Zn metals since the results were qualitative and difficult to record and interpret due to low inhibitor content. XPS spectra were recorded for Cu and Zn metals and Cu-10Zn and Cu-40Zn alloys.

Additionally, another set of experiments was conducted to record *in situ* ATR-FTIR spectra during the immersion of a metal sample in an organic solvent containing an organic inhibitor. Tetrahydrofuran (THF) was used instead of aqueous solvent to avoid the effect of the solvent on the peak shape. Spectra were recorded for Cu and Zn as a function of immersion time in the THF solvent containing MBI and MMBI inhibitors.

3.3.1. Fourier transform infrared spectroscopy

The infrared vibrational spectroscopic technique has been widely used to identify functional groups in a molecule since each specific chemical bond often has a unique energy absorption band. IR spectra of the Imd, MBI, and MMBI compounds, adsorbed on a copper substrate in 3 wt% NaCl solution have been examined (Fig. 6). In addition, the spectra of copper surface exposed to NaCl (designated as the blank sample) and solid powder inhibitor compounds (labelled (s)) are presented as a reference. The assignment of the IR bands is given in Table 4.

The IR spectrum of the sample in the absence of inhibitors, designated as blank, distinguishes three distinct frequency ranges

[4] Due to the variety of complex shapes of anodic curves, it would be difficult to determine the exact values of breakdown potentials for all the materials investigated.

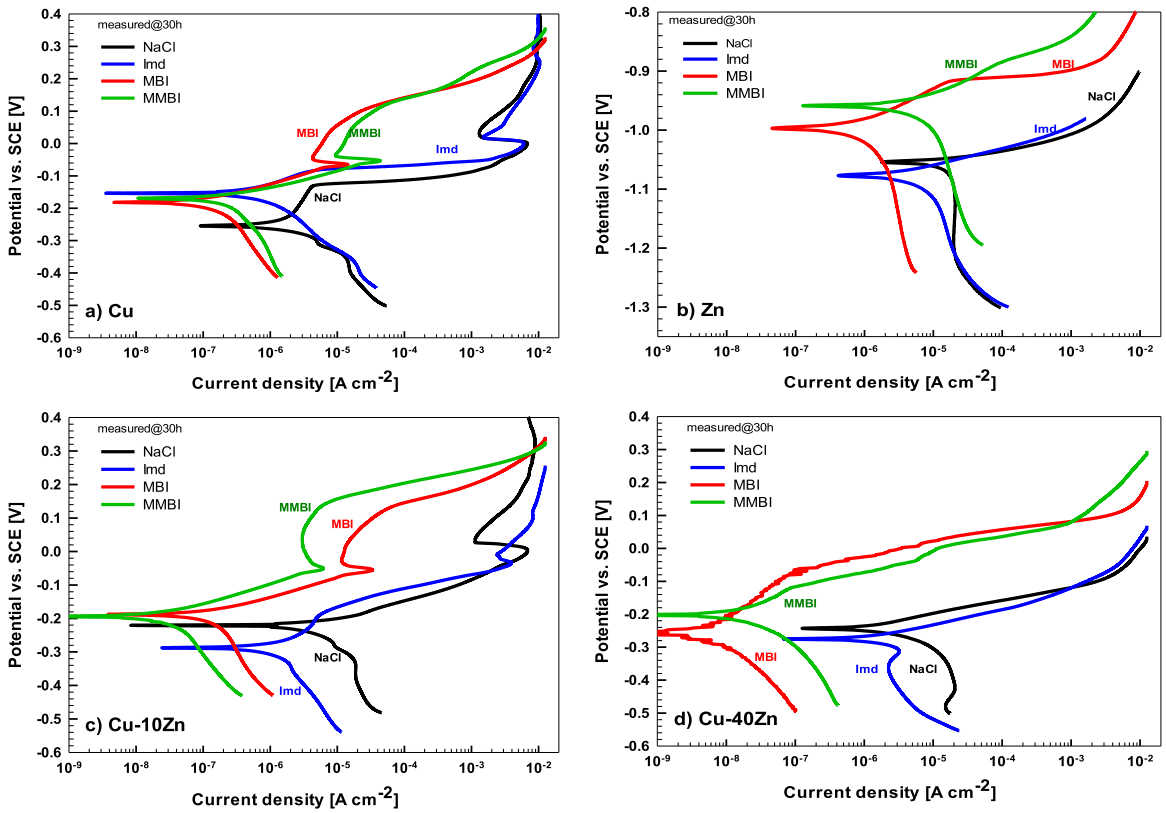

Fig. 5. Potentiodynamic polarisation curves of (a) Cu, (b) Zn, (c) Cu-10Zn, and (d) Cu-40Zn recorded in 3 wt% NaCl with and without added 1 mM Imd, MBI, and MMBI. Stabilisation time at the E_{oc} was 30 h. Electrochemical parameters are given in Table 3.

Table 3
Electrochemical parameters deduced after 30 h stabilisation at E_{oc} for Cu, Cu-10Zn, Cu-40Zn, and Zn in 3 wt% NaCl with and without 1 mM inhibitor added (Fig. 5). Mean values and standard deviations are given. The current density values at the selected potentials are presented to compare the behaviour in the anodic region (last column).

Solution	Electrochemical parameter		
	E_{corr} [V]	j_{corr} [μA/cm^2]	$j_{E=0\ V}$ [μA/cm^2]
	Cu		
NaCl	−0.243 ± 0.042	2.050 ± 0.295	6797 ± 3150
NaCl+Imd	−0.173 ± 0.023	0.855 ± 0.485	4607 ± 2228
NaCl+MBI	−0.168 ± 0.011	0.123 ± 0.030	7 ± 5
NaCl+MMBI	−0.194 ± 0.035	0.228 ± 0.066	13 ± 0.2
	Cu-10Zn		
NaCl	−0.243 ± 0.021	4.960 ± 0.693	6180 ± 3503
NaCl+Imd	−0.284 ± 0.017	1.245 ± 0.069	2974 ± 245
NaCl+MBI	−0.190 ± 0.020	0.155 ± 0.030	13 ± 0.7
NaCl+MMBI	−0.188 ± 0.026	0.042 ± 0.009	5 ± 2
	E_{corr} [V]	j_{corr} [μA/cm^2]	$j_{E=-0.2\ V}$ [μA/cm^2]
	Cu-40Zn		
NaCl	−0.218 ± 0.008	3.700 ± 0.650	7 ± 3
NaCl+Imd	−0.263 ± 0.004	1.530 ± 0.495	52 ± 32
NaCl+MBI	−0.236 ± 0.012	0.033 ± 0.020	0.04 ± 0.02
NaCl+MMBI	−0.221 ± 0.009	0.053 ± 0.030	0.2 ± 0.1
	E_{corr} [V]	j_{corr} [μA/cm^2]	$j_{E=-0.95\ V}$ [μA/cm^2]
	Zn		
NaCl	−1.056 ± 0.018	19.67 ± 0.76	5044 ± 333
NaCl+Imd	−1.067 ± 0.032	8.379 ± 3.833	2330 ± 747
NaCl+MBI	−1.005 ± 0.017	0.626 ± 0.543	4 ± 0
NaCl+MMBI	−0.949 ± 0.006	6.258 ± 0.680	3 ± 2

characteristic of copper oxidation under atmospheric conditions and in aerated chloride solutions (Fig. 6). In the low-frequency region (denoted as 1) (Fig. 6a), the peaks related to the Cu–O stretching were observed around 460 cm^{-1}, 530 cm^{-1}, and 585 cm^{-1} [61,62], followed by the intense vibration at 640 cm^{-1} corresponding to the Cu_2–O stretching, which is in good agreement with the previous results [2,61,62]. The second characteristic region between 1000 and 800 cm^{-1} (denoted as 2 in Fig. 6a) is related to the presence of clinoatacamite (hydroxychloride polymorph, $Cu_2(OH)_3Cl$) formed as the corrosion product at the Cu surface. The third characteristic region between 3500 and 3200 cm^{-1} (region 3) is due to the hydroxyl stretching [63,64].

Alteration in vibrational frequencies upon the addition of inhibitor was expected due to the interaction between inhibitor molecules and the copper surface. However, after exposure of copper specimen to imidazole-containing solution, no significant change occurred compared to the blank sample, except that the Cu_2–O stretching vibration at 640 cm^{-1} vanished, indicating the suppression of Cu(I) oxide (Fig. 6a). The small peak located around 1090 cm^{-1} could correspond to a certain degree of adsorption, i.e., incomplete coverage by the inhibitor, however, the peak around 740 cm^{-1} characteristic of the aromatic C–H stretching is missing. Accordingly, it can be concluded that Imd did not sufficiently adsorb on the copper surface to be detected by FTIR (*vide infra* XPS results), leading to insufficient corrosion protection (Table 3).

On the other hand, for the Cu specimens prepared in the presence of MBI (Fig. 6b), the band at 2975 cm^{-1} can be associated with the C–H stretching of methyl and that at 1491 cm^{-1} is assigned to the C–C stretching vibrations in the aromatic ring [65,66]. Moreover, the frequency of around 740 cm^{-1} is assigned to the out-of-plane bending vibration of the phenyl ring [66]. In the high-frequency range, the peak around 3320 cm^{-1}, corresponding to the O–H stretching, indicates the hydroxylated surface [66,67]. Furthermore, direct evidence of the presence of MBI is the imino-group peak at 1627 cm^{-1} corresponding to C═N, and peaks at 1366 cm^{-1} and 1270 cm^{-1} corresponding to C–N.

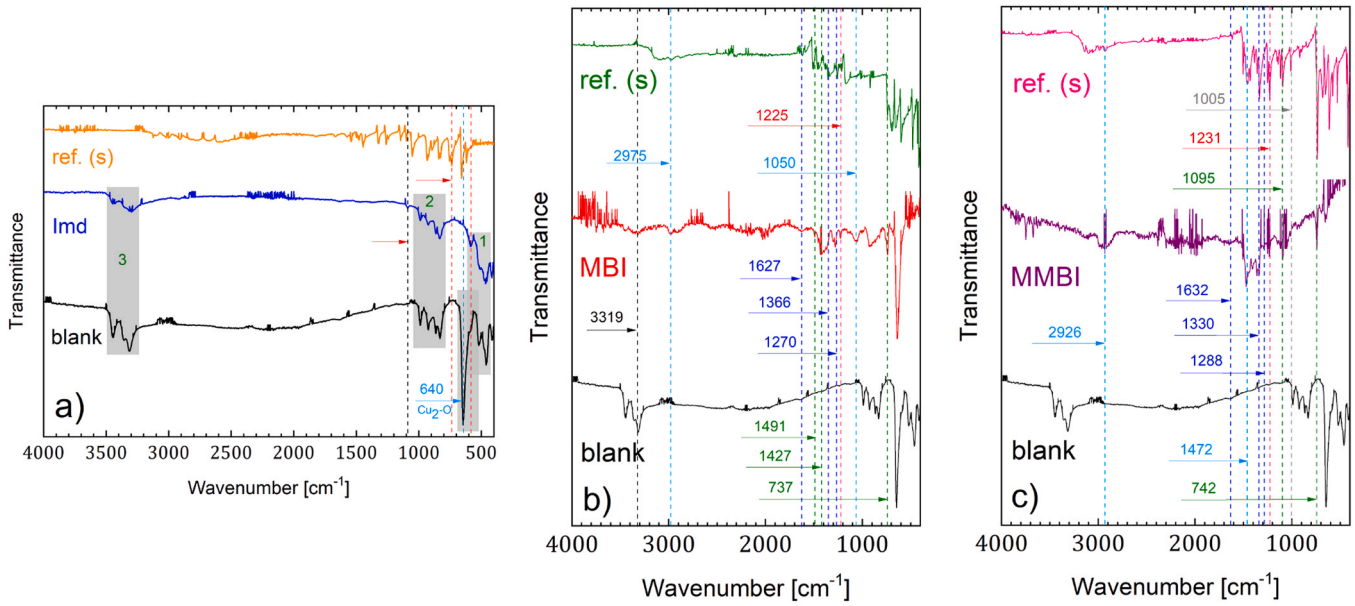

Fig. 6. FTIR spectra recorded for Cu samples immersed for 30 h in 3 wt% NaCl with and without added 1 mM (a) Imd, (b) MBI, and (c) MMBI. Spectra recorded in blank 3 wt% NaCl are also presented together with reference spectra for inhibitor compounds. The positions of characteristic bands denoting the reference C–C, C–N, and C–S bonds are presented by vertical lines.

Table 4
The list of characteristic bands in the FTIR spectra of Figs. 6 and 7.

Wave number (cm^{-1})	Vibration (Cu sample)	Wave number (cm^{-1})	Vibration (Zn sample)
460, 530, 585	Cu–O stretching of CuO	559	Zn–O stretching
640	Cu–O stretching of Cu_2O		
737/742	C–H out-of-plane bending	759/743/741	C–H out-of-plane bending
1050	Inhibitor–Cu interaction	1090	C–H in-plane bending
800–1000	OH^- bending	670	C═C bending
1130–1340	N–CS–N	1606	C═C or C═N stretching
1225/1231	C═S stretching	1226/1236	C═S stretching
1427, 1491	C═C–C stretching	1400–1600	C═C–C stretching
1627/1632	C═N stretching	1617/1612	C═N stretching
1270, 1366	C–N stretching	1282/1277/ 1289, 1319	C–N stretching
1472	$-CH_2$, $-CH_3$ scissoring	1475	$-CH_2$, $-CH_3$ scissoring
2930	C–H stretching of methyl	2930	C–H stretching of methyl
3200–3500	O–H stretching	3200–3500	O–H stretching

These results are in accordance with the previous results related to experimentally obtained and calculated stretching vibrations [2,66,67,68,69].

Finally, the N–CS–N stretching arising from the C═S functional group occurs in the 1340–1130 cm^{-1} range [67,70]. The powdered MBI compound, used as a reference, exhibits this peak around 1160 cm^{-1}, which disappeared for adsorbed MBI together with the appearance of the new vibration at 1050 cm^{-1}, indicating the opening of the C═S double bond, probably due to molecular adsorption bonding via its S atom (e.g. thiolate adsorption mode). Also, the vibration at 1225 cm^{-1} can be assigned to the C═S stretching. The existence of adsorbed thiones (C═S) and thiolates (C–S–Cu), but not thiols (C–SH), has a solid foundation in DFT calculations [24]. It is noteworthy to mention that the assignment of the band due to the C–S stretching vibration is complicated in infrared spectroscopy, whereas the C–S (thiolate) stretching vibrations exhibit strong spectral activity in Raman spectra, which makes it easy to identify [69].

Compared to MBI, the MMBI molecule has an additional methyl functional group attached to the nitrogen atom of the imidazole ring. Hence, it is reasonable to expect similar vibrational frequencies to those of the MBI sample. The strong absorption at 1472 cm^{-1} and pronounced peak around 2930 cm^{-1} are attributed to the methyl group [65,71]. In addition, the band located at 1095 cm^{-1} is associated with the C–H in-plane bending. The presence of the inhibitor on the metal surface was confirmed by vibration frequency at 1632 cm^{-1}, designated to the C═N imino group, and absorptions around 1330 cm^{-1} and around 1290 cm^{-1} assigned to the C–N group. The presence of inhibitors is also evidenced by the C–H in-plane bending mode of benzene [68] and the aromatic C–H out-of-plane bending vibration at 742 cm^{-1}. Finally, the absence of the band at 1005 cm^{-1}, evident in the MMBI reference spectrum, could probably be due to the chemisorption.

The spectra of the Zn sample after exposure to 3 wt% chloride-containing solutions with and without added Imd, MBI, and MMBI are presented in Fig. 7. Characteristic absorption of Zn–O at 559 cm^{-1} is evidenced for the blank sample (Fig. 7a) [72]. The Zn sample treated with Imd, unlike the Cu treated with Imd, shows a variety of vibrations. The existence of an aromatic ring is readily determined from the C–H and C═C–C ring-related vibrations. The frequency at 759 cm^{-1} is assigned to the C–H out-of-plane bending [65] followed by aromatic C–H in-plane bending, C═C bending, and C═C stretching of the five-membered heterocyclic ring [65–67] at 1090 cm^{-1}, 670 cm^{-1}, and 1606 cm^{-1}, respectively. It is sometimes difficult to assign a double-bonded nitrogen group, such as the imino group (C═N), because it exhibits absorption close to the C═C stretching region [65]. Therefore, the evolution of absorption at 1606 cm^{-1} cannot be unambiguously assigned to either C═N or C═C stretching vibrations [2,65,73]. The evidence of secondary amine (C–N) stretching vibrations appearing at 1282 cm^{-1} and 1319 cm^{-1} confirms the presence of Imd on the surface of the zinc substrate [65,66,74]. Despite the strong adsorption of Imd on the surface of Zn, which is in correlation with electrochemical measurements after 1 h of immersion, a degree of inhibition significantly diminished after 30 h of immersion (Fig. 5).

The spectra of MBI (Fig. 7b) and MMBI (Fig. 7c) for Zn are characterised by well-defined sharp peaks compared to those for Cu. The

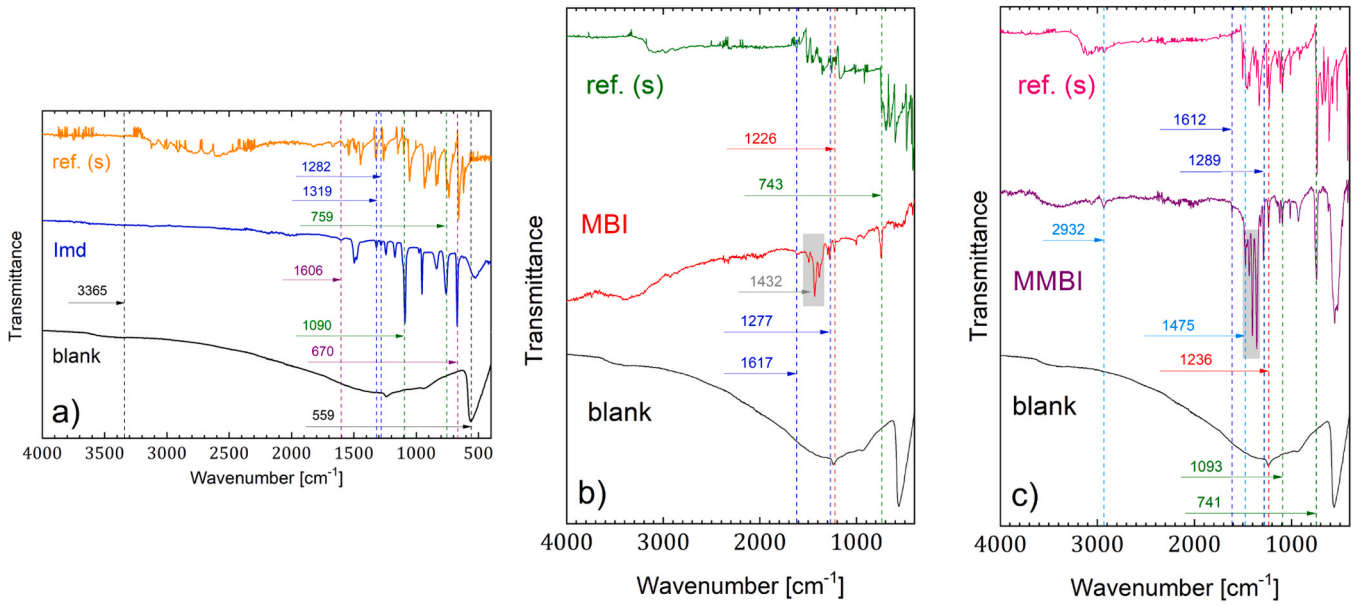

Fig. 7. FTIR spectra recorded for Zn samples immersed for 30 h in 3 wt% NaCl with and without added 1 mM (a) Imd, (b) MBI, and (c) MMBI. Spectra recorded in blank 3 wt% NaCl are also presented together with reference spectra for inhibitor compounds. The positions of characteristic bands of the reference C–C, C–N and C–S bonds are presented by vertical lines.

absorption bands for both Zn and Cu are consistent. The aromatic ring C=C–C vibrations, centred around 1600 cm^{-1} and 1400 cm^{-1}, appear as a pair of band structures with some splitting (marked with the grey square) [65]. Further, 743 cm^{-1} was designated to aromatic C–H out-of-plane bending vibration [65,66]. The imino group (C=N) is attributed to the stretching vibration at 1617 cm^{-1} [67,73]. Further, the absorption at 1277 cm^{-1} corresponds to aromatic secondary amine stretching (C–N) [65]. The evidence of the presence of MBI on the surface of zinc is complemented by the existence of C=S stretching vibration at 1226 cm^{-1} in the case when it is a part of nitrogen-containing thiocarbonyl derivatives (N–CS–N) (Fig. 7b) [67].

The spectrum collected for MMBI (Fig. 7c) exhibits frequencies around 740 cm^{-1} and 1090 cm^{-1}, which can be associated with the aromatic C–H out-of-plane and the C–H in-plane bending vibrations, respectively [65]. A comparison of the spectrum of MBI (Fig. 7b) with the spectrum of MMBI (Fig. 7c) shows a distinctly different absorption within the marked grey region. Namely, the strong absorption at 1475 cm^{-1} (Fig. 7c) is indicative of the scissoring of a methylene/methyl group [65,71], consistent with the molecular structure of MMBI containing the methyl group (Fig. 1c). Additionally, the C–H stretching vibration around 2930 cm^{-1} is characteristic of the methyl group. The intense peaks at 1289 cm^{-1} and 1612 cm^{-1} can be attributed to the stretching vibration of aromatic amine (C–N) and imino group (C=N), respectively [65–67,74]. Finally, the band at 1236 cm^{-1} corresponds to the stretching vibration of C=S [67].

It should be emphasised that, despite being the technique for routine analysis, it was not straightforward to record FTIR spectra due to a very small amount of the inhibitors on the substrate surface. Therefore, this technique was used only for the detection of functional groups, providing complementary and confirmatory sample information. Further information on the chemical composition and chemical speciation were obtained quantitively based on the XPS analysis.

Fig. 8 shows ATR-FTIR spectra of MBI and MMBI on pure Cu and Zn films deposited on the Ge crystal exhibiting the interaction kinetics. The peaks at 910–920, 1080–1090 and 2870–2980 cm^{-1} originate from C–C, C–N, and C–H, respectively. The spectra of both inhibitors exhibit clear peaks originating from the molecular backbone, indicating an interaction of the inhibitor with the surfaces. However, the higher peak intensity obtained for MBI than MMBI may indicate slightly higher

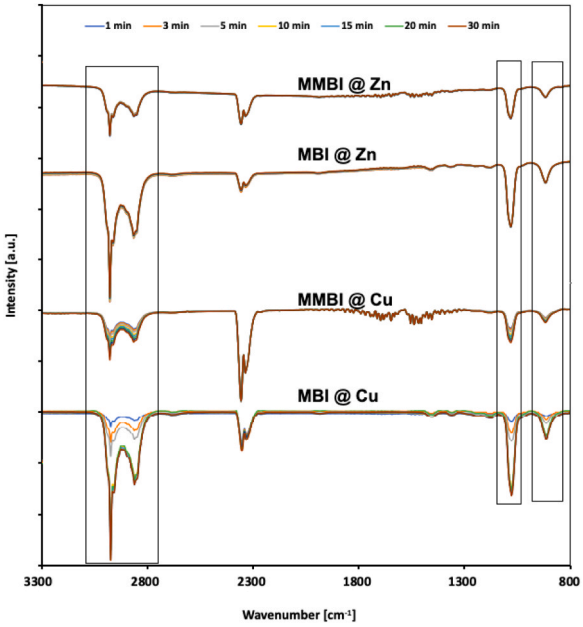

Fig. 8. In-situ FTIR spectra of Cu and Zn samples exposed to 1 mM inhibitors dissolved in THF. From bottom to top: MBI on Cu, MMBI on Cu, MBI on Zn, and MMBI on Zn. The peaks marked with rectangles are discussed in the text.

coverage of MBI on both surfaces. Also, increasing peak intensity of both inhibitors by time on Cu surfaces indicates a gradual increased surface coverage, whereas the relatively similar peak intensities of 20 and 30 min exposure imply saturation after 20 min. However, the peak intensities of both inhibitors are similar on Zn surfaces, which could be due to quick but limited interactions of inhibitors with the surfaces.

3.3.2. *X-ray photoelectron spectroscopy*

The chemical composition of Cu, Zn, and Cu-*x*Zn alloy surfaces after immersion for 30 hours in NaCl with and without 1 mM Imd, MBI, and MMBI are presented in Table 5. A high oxygen content on the Cu surface

Table 5
Chemical composition deduced from XPS survey spectra of layers formed during 30 h immersion of Cu, Cu-10Zn, Cu-40Zn, and Zn in 3 wt% NaCl with and without 1 mM inhibitor added.

Element	Atomic %							
	NaCl				**NaCl + Imd**			
	Cu	Cu-10Zn	Cu-40Zn	Zn	Cu	Cu-10Zn	Cu-40Zn	Zn
C	54.7	29.9	28.2	21.6	49.1	29.0	48.8	46.6
O	26.0	35.7	38.6	53.7	27.5	34.8	19.3	16.1
N	-	1.3	-	-	2.7	5.1	17.7	21.9
Zn	-	1.7	28.3	24.7	-	3.3	9.9	15.4
Cu	12.1	28.5	4.2	-	13.4	20.5	2.7	-
Cl	3.1	2.9	0.7	-	7.3	7.3	1.6	-
S	-	-	-	-	-	-	-	-
	NaCl + MBI				**NaCl +MMBI**			
C	68.8	68.8	67.5	70.4	68.4	67.0	75.8	72.1
O	7.0	5.5	8.7	6.2	6.8	4.5	-	4.8
N	10.6	14.0	11.8	12.6	12.5	12.8	12.6	12.2
Zn	-	-	1.3	4.0	-	0.5	4.3	4.1
Cu	5.5	4.8	3.8	-	3.3	4.1	0.2	-
Cl	-	-	1.6	-	-	-	-	-
S	8.2	7.0	6.9	6.8	9.0	11.0	7.1	6.8

indicates that after immersion in NaCl, the surface is covered by an oxide layer (Cu_2O). Some chloride was detected, indicating the formation of an oxychloride compound. For the Zn sample, no chloride was detected after immersion in NaCl, while the high oxygen content indicates the formation of zinc oxide. Although ZnO is thermodynamically stable above pH 8, in the pH range between 7 and 10, zinc dissolution can result in the formation of Zn oxide or oxychloride (reactions 31 and 32) [60].

The surface of the Cu-10Zn sample contained high Cu content and also some Zn, while *vice versa* was valid for Cu-40Zn, in accordance with the increasing content of Zn in the alloy. Chloride was identified on both layers but with a higher content on the Cu-10Zn samples. Reduced Cl content at the surface of Cu-40Zn and Zn compared to Cu-10Zn and Cu may be related to the high solubility of $ZnCl_2$ ($ZnCl_2$ is highly soluble, $CuCl_2$ is soluble, and CuCl is only sparingly soluble in water). In all cases, an abundant carbon content is related to adventitious carbon (Table 5).

Adding Imd in the NaCl solution caused several changes at the surface. For Cu-40Zn and Zn, metal concentrations significantly decreased. Nitrogen originating from imidazole was detected for all four materials, but its concentration was up to 5 times larger on Cu-40Zn and Zn samples than on Cu-10Zn and Zn. These results indicate that the surface is covered by an imidazole-based mixed organic-oxide layer. Chloride concentration increased twofold on Cu and Cu-10Zn compared to that in NaCl, suggesting that chloride is incorporated in the surface layer. Since copper chloride-containing compounds are highly soluble, it can be hypothesised that the content of dissolved chloride species is significantly higher; therefore, XPS data confirm that Imd is not an efficient inhibitor for Cu and Cu-10Zn. In contrast, no Cl was detected in the layer formed on Zn. The lack of Cl detection and high N and low O concentrations suggest that Imd on Zn and Cu-40Zn forms an organic-containing layer which can prevent chloride ingress, opposite to that on Cu and Cu-10Zn. This observation may also be related to the higher stability of ZnO in a more alkaline solution of pH 8.3 caused by adding imidazole. At pH 8.3, ZnO is more stable than in near-neutral (or slightly acidic) NaCl solutions with and without the addition of two mercapto-based inhibitors (pH = 5.6–5.7) [58].

Even more significant changes are observed after immersion in MBI and MMBI containing NaCl solutions (Table 5). Carbon concentration in all layers exceeded 67 at%, while oxygen was reduced to the range of 4.5–8.7 at%. Nitrogen was detected on all surfaces. The changes were more pronounced for Cu and Cu-10Zn in the presence of MBI and MMBI than Imd. Further, sulphur appeared for the mercapto-based inhibitors with concentrations of 6.8–11 at%. Cl, Cu, and Zn contents were

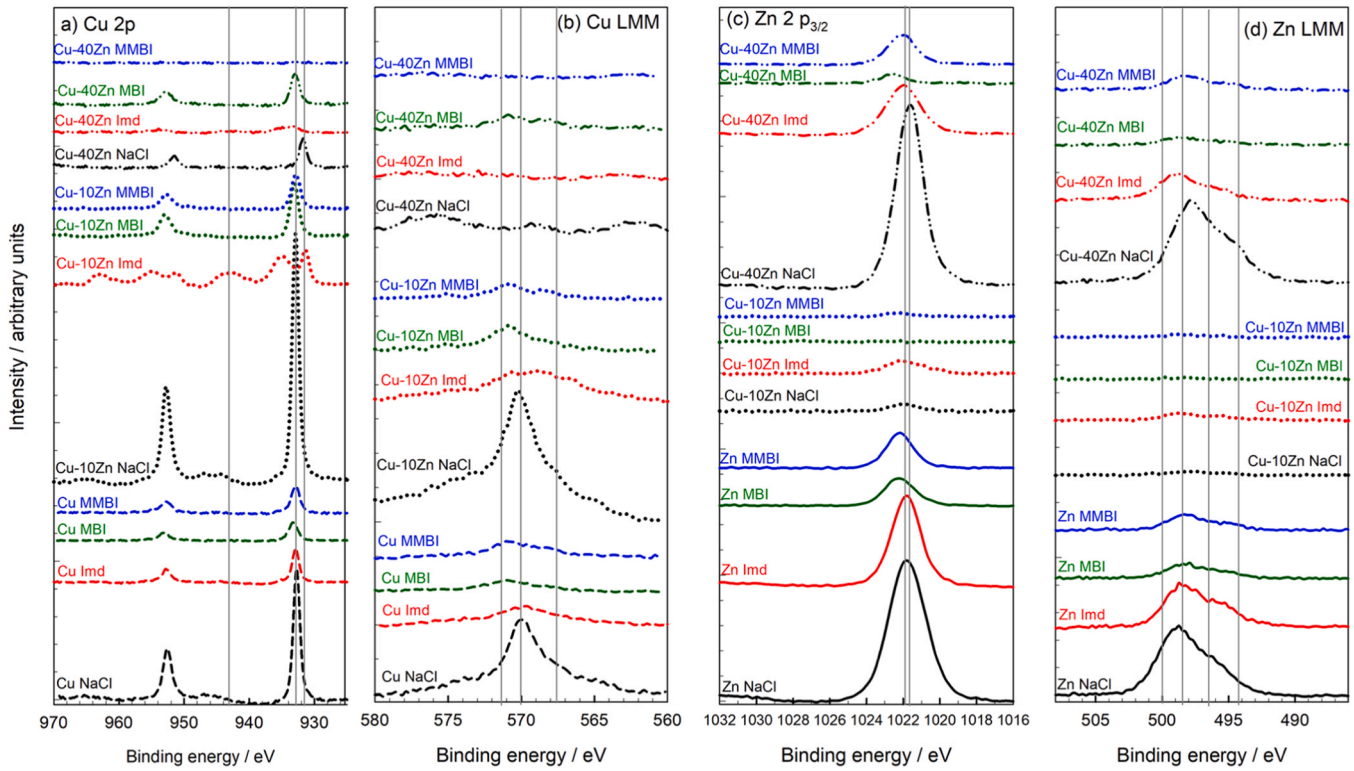

Fig. 9. High-energy resolution XPS spectra of (a) Cu 2p, (b) Cu Auger [$L_3M_{4,5}M_{4,5}$], (c) Zn 2p, and (d) Zn Auger [$L_3M_{4,5}M_{4,5}$] of Cu, Cu-10Zn, Cu-40Zn, and Zn samples immersed for 30 h in 3 wt% NaCl with and without 1 mM Imd, MBI, and MMBI. Spectra were not normalised on the intensity scale, but the position of binding energy was adjusted to the C 1 s peak at 284.8 eV. Vertical lines denote the position of reference species, as described in the text.

strongly reduced, indicating that the organic layers containing inhibitor species were formed.

Figs. 9–11 show the chemical speciation of the elements based on the high-energy resolution XPS spectra, aligned according to the position of C 1 s peak (284.8 eV). The spectra were not normalised on the intensity scale to better present the intensity of individual peaks relative to different substrates and inhibitors. After 30 h immersion in 3 wt% NaCl solution, Cu $2p_{3/2}$ peak was located at 932.5 eV and is consistent with the formation of cuprous Cu(I) oxide (Fig. 9a). Cupric Cu(II) species, which would be identified by a satellite peak *ca.* 10 eV above the Cu $2p_{3/2}$ peak, were not detected. The presence of cuprous species is also corroborated by the position of the Auger [Cu($L_3M_{4,5}M_{4,5}$)] peak at 569.9 eV (Fig. 9b); metallic Cu, which shows an Auger peak at 567.6 eV, is absent [75]. The centre of the Zn $2p_{3/2}$ peak was located at 1021.5 eV (Fig. 9c) and is consistent with the formation of both Zn and ZnO [75]. However, the position of the centre of Auger [Zn($L_3M_{4,5}M_{4,5}$)] peak at 498.3 eV indicates that the major product is ZnO (Fig. 9d). Considering a rather broad low-binding energy envelope, another peak at 496.5 eV related to ZnO_x could also be present. The peak of Zn metal expected at 494.9 eV is absent [75]. Each Auger [$L_3M_{4,5}M_{4,5}$] Cu and Zn peak can be described by at least four functions, each consisting of a Gaussian/Lorentzian part and an asymmetric tail function [75]. The Cu-10Zn alloy exhibited similar spectra as Cu, whereas the Cu-40Zn alloy expressed a smaller intensity of Cu peaks and a larger intensity of Zn peaks (Fig. 9), consistent with their relative contents in the alloy. Thus, the layer formed on Cu-10Zn is predominantly Cu_2O with a small content of ZnO, and that on Cu-40Zn is predominantly ZnO with a small content of Cu_2O, as reported previously [75]. As evidenced in Fig. 9, the position of Auger peaks is somewhat dependent on the substrate material [75,76].

When the NaCl solution contained inhibitors, the intensity of Cu and Zn peaks was significantly reduced. In the [Cu($L_3M_{4,5}M_{4,5}$)] spectra, the formation of the inhibitor-containing layer can be recognised by the broadening of the Auger peaks due to the formation of the peak at 571.8 eV (Fig. 9b). In the [Zn($L_3M_{4,5}M_{4,5}$)] spectra, the related feature can be observed by the widening of the high energy envelope which could be described by the peak at 500.2 eV (Fig. 9d). Similar results were reported previously by our group for Cu, Zn, and Cu-*x*Zn alloys in NaCl containing benzotriazole [76].

Carbon 1 s peaks were centred at 284.8 eV for all samples analysed (Fig. 10a). Compared to the spectra recorded after immersion in blank NaCl solution, the presence of the organic inhibitors led to an increase of the full width at half maximum, indicating the contribution of organically bonded species, i.e., C−O (286.5 eV), C−N (286.1 eV), C−S (286.9 eV), C═N (287.5 eV), and C═O (288.4 eV) at the high-binding energy envelope. The intensity of C 1 s peak increased from blank NaCl to NaCl+MMBI, indicating an increasing concentration of carbon in the surface layer. The opposite trend was observed for oxygen (Fig. 10b); the O 1 s spectra were more intense for the samples immersed

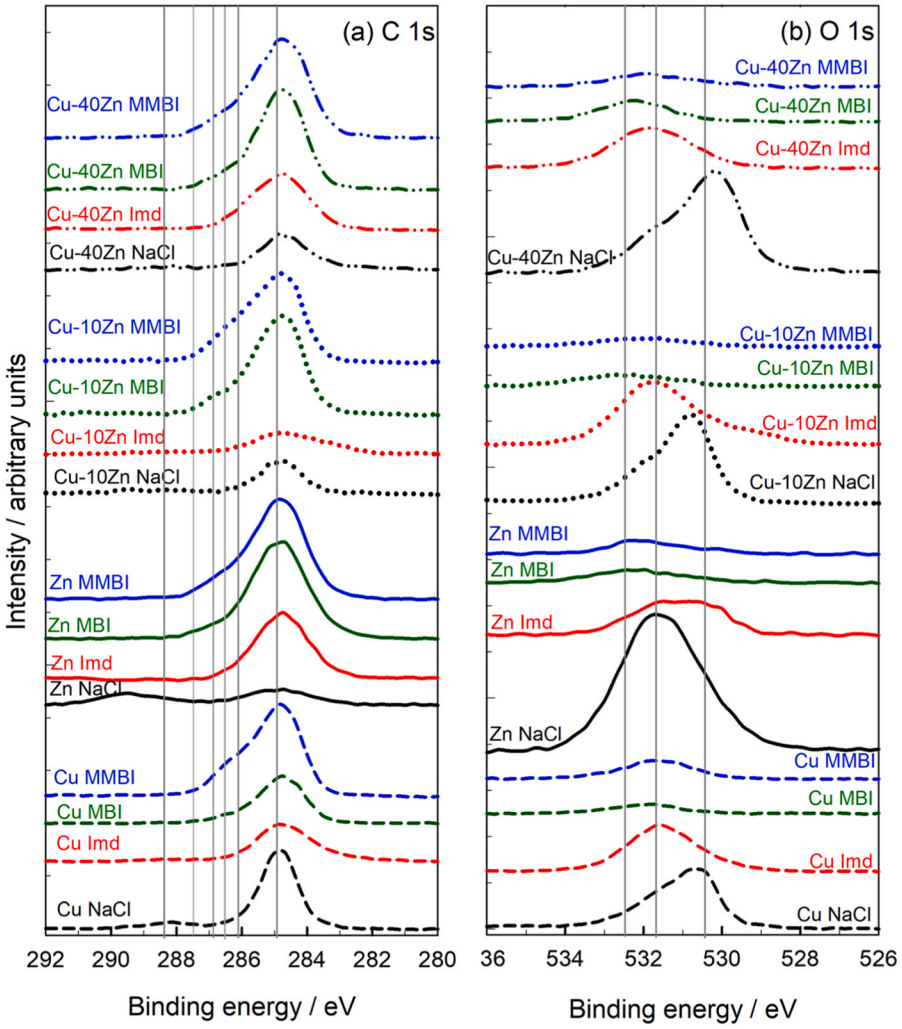

Fig. 10. High-energy resolution XPS spectra of (a) C 1 s and (b) O 1 s of Cu, Cu-10Zn, Cu-40Zn, and Zn samples immersed for 30 h in 3 wt% NaCl with and without 1 mM Imd, MBI, and MMBI. Spectra were not normalised on the intensity scale, but the position of binding energy was adjusted to the C 1 s peak at 284.8 eV. Vertical lines denote the position of reference species, as described in the text.

in the blank NaCl and NaCl+Imd, while the samples exposed to NaCl+MBI and NaCl+MMBI exhibited smaller peak intensities due to the prevalence of organic species on the surfaces as indicated by chemical composition (Table 5). It is noteworthy that for the samples immersed in NaCl containing Imd, a shift of peak centre to higher binding energy occurred, i.e., from 530.4–530.6 eV to 531.6–531.8 eV, which reflects the formation of a mixed Imd-containing organic layer. The binding energy of 532.5 eV is related to adsorbed water molecules.

Based on FTIR spectra, it was concluded that the MBI and MMBI inhibitors are bonded to the Cu surface. The presence of both C═N and C−N bonds was evident in FTIR spectra (Fig. 6). In contrast, C═S and C−S bonds were difficult to unambiguously confirm by FTIR due to overlapping with other vibrations (Fig. 6). Therefore, N 1 s and S 2p XPS spectra are of particular interest since they offer additional insight into the understanding of the bonding of inhibitor molecules to the metal surfaces [19]. Nitrogen is present in all three inhibitors, but sulphur is contained in only mercapto-based inhibitors. A previous study showed that two-component peaks were identified in the N 1 s spectrum for mercapto-based MBI: the peak at 400.0−400.6 eV ascribed to C−NH−C (pyrrole N) and the peak at 398.8−399.0 eV to C═N−C (pyridine N) [19]. Angle-resolved XPS spectra showed that pyridine N atoms point towards the metal surface, and pyrrole N atoms are oriented upwards. The existence of both pyrrole and pyridine nitrogen was taken as experimental proof that molecules are present in thiolate form [19]. In contrast, non-mercapto benzimidazole inhibitor showed only one peak at 400 eV [19]. Nitrogen spectra in Fig. 11a present several important issues. When the samples were immersed in NaCl+Imd, only one peak appeared in N 1 s spectra centred at *ca.* 398.8 eV (Fig. 11a). The intensity of this peak, ascribed to pyridine C═N−C bond, increased from Cu, followed by alloys, to Zn metal, in accordance with Table 5. It is not entirely clear why only one peak, ascribed to pyridine N, is resolved in the XPS spectrum for the sample immersed in NaCl containing Imd. FTIR spectra could not identify the adsorption of Imd at the surface (Fig. 6a). It is, therefore, difficult to reconcile the results of these two techniques (FTIR requires a sufficiently large amount of compound, while XPS has a nanometric analysis depth). Further, the ratio of pyrrole and pyridine peaks depends on the take-off angle, as shown previously [19]. Nonetheless, these results show that Imd is present on the surface of Zn and Cu-40Zn more abundantly than on Cu and Cu-10Zn, in line with FTIR results (Figs. 6,7). In terms of corrosion efficiency, however, its presence does not assure long-term protection (Fig. 5, Table 3).

Two peaks centred at 398.8 eV and 400.6 eV for mercapto-based compounds appeared, indicating the presence of both thione and thiolate species, as suggested previously [2,19]. For MBI on Cu and Zn, the pyridine C═N−C peak at 398.8 eV prevailed over pyrrole C−NH−C peak at 400.6 eV. For MMBI, the pyrrole peak prevailed over the pyridine peak; this observation is consistent for all materials. Similar spectra for MBI with two nitrogen peaks were obtained by Finšgar [32], who observed the prevalence of the peak at lower E_b closer to the interface with the substrate, similar to our previous reports [2,19].

It is also important to analyse S 2p spectra, as the corresponding C═S and C−S bonding is difficult to resolve in FTIR spectra (Figs. 6,7). In XPS spectra, the centre of the S 2p peak is located at 162.2 eV (Fig. 11b). Most S 2p spectra are not well resolved into $2p_{3/2}$ and $2p_{1/2}$ peaks due to a small chemical shift among them (1.18 eV) and are usually interpreted as a single peak, which represents a doublet [19,32]. However, spectra recorded for the mercapto-based samples exhibit two well-resolved peaks (162.2 eV and 163.6 eV), possibly indicating the presence of

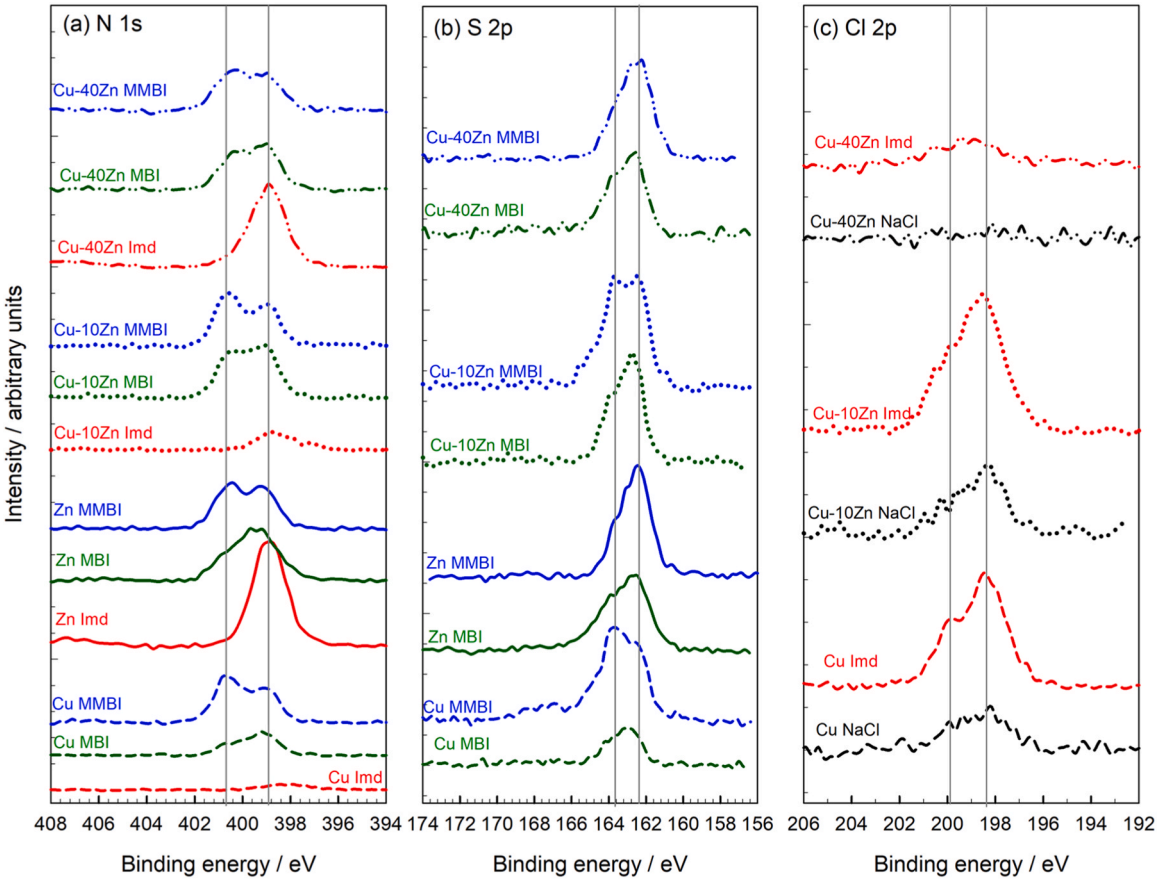

Fig. 11. High-energy resolution XPS spectra of (a) N 1 s, (b) S 2p, and (c) Cl 2p of Cu, Cu-10Zn, Cu-40Zn, and Zn samples immersed for 30 h in 3 wt% NaCl with and without 1 mM Imd, MBI, and MMBI. Spectra were not normalised on the intensity scale, but the position of binding energy was adjusted to the C 1 s peak at 284.8 eV. Vertical lines denote the position of reference species, as described in the text.

both C−S and C═S species, associated with the presence of thiolate and thione (Fig. 11a). The spectrum for MBI is similar to our previous report, where the peak centred at 162.3 eV was ascribed to the S−Cu bonding [2]. Literature data allow the postulation of two different sulphur species. However, the issue is not well clarified: for 2-mercaptobenzothiazole, the S 2p peak at 164 eV was ascribed to thiolate [77], peak at 164.5 eV to endocyclic sulphur atom, and at 162.3 eV to exocyclic sulphur atom [78]; for 3-amino-5-mercapto-1,2,4,-triazole the peak at 162 eV was related to thiolate group and that at 164 eV to thione tautomer [79]. Recently, Wu et al. ascribed the S $2p_{3/2}$ at 161.8 eV to the S−Cu bond, whereas the peak at 162.4 eV is related to S in a non-bonded MBI molecule [33]. Finšgar reported the presence of two peaks in the MBI molecule corresponding to a non-bonded (162.3 eV) and bonded (163.5 eV) molecule [32]. It would be reasonable to assume that peaks at higher E_b in N 1 s and S 2p spectra are related to each other and represent the mixture of adsorbed thiones and thiolates.

Fig. 11c shows Cl 2p spectra for Cu and Cu-10Zn samples immersed into the blank NaCl and Imd-containing solutions. For other samples, the Cl signal was not detected, presumably due to the higher solubility of zinc-chloride than copper-chloride complexes, as discussed above. Similar to S 2p spectra, the splitting between $2p_{3/2}$ and $2p_{1/2}$ peaks is rather small (1.3–1.5 eV). The peaks at 198.4 eV and 199.8 eV may be ascribed to copper chloride and oxychloride compounds, respectively, reported previously at E_b between 198.4 eV and 199.4 eV [19].

3.4. DFT calculations

Adsorption characteristics of imidazole and 2-mercaptobenzimidazole on metallic and oxidised Cu surfaces have already been studied with DFT calculations in previous publications [2,20,22,24,42, 80–89]. In contrast, the adsorption of azoles on zinc and brass surfaces [90,91] has been much less explored by DFT methods than on Cu surfaces. Here, we extend the previous calculations by considering the adsorption on various models of zinc and copper surfaces (cf. Fig. 2) and, in addition to imidazole and 2-mercaptobenzimidazole, also characterise the adsorption of 2-mercapto-1-methylbenzimidazole.

3.4.1. Preliminaries

MBI and MMBI can exist in two tautomer forms: thiol (R−SH), labelled as SH-BimH and SH-BimMe for MBI and MMBI, respectively, and thione (R═S), labelled as S-$BimH_2$ and S-BimMeH (Fig. 1 and Table 1). Thione is significantly more stable than thiol, by about 0.5 eV [21,24]. Hence, MBI and MMBI molecules exist almost exclusively in a thione form at room temperature. Furthermore, it was demonstrated in our previous publication [24] that adsorbed thiol would dissociate immediately via cleavage of the S−H bond, resulting in adsorbed thiolate. For these reasons, only adsorbed thiones and thiolates were considered in calculations, and all adsorption energies of mercapto molecules are calculated with respect to solvated thione tautomers in the (implicit) aqueous solvent.

The adsorption of azoles on copper surfaces has been studied in detail by DFT calculations in the literature [6,24,45,81-83,92]. An essential insight of these studies is that the adsorption bonding of dissociated molecules with the cleaved X–H bond is much stronger than those of intact molecules. However, the thermodynamic stability of the two adsorption modes is not as different due to the energy cost associated with the bond-breaking in dissociative adsorption. On bare copper surfaces, the dissociation barrier for the N–H bond cleavage is about 1 eV [24,93]. However, on oxidised copper surfaces, the surface O* and OH* groups considerably lower this activation barrier to values below 0.1 eV [82,85]. In this context, imidazoles behave differently from triazoles and mercaptoazoles due to their specific molecular geometry. In particular, calculations demonstrate that for the X–H bond breaking to be thermodynamically favoured, the adsorbed molecule needs to bond to the surface with at least two of its atoms [82,83]. However, imidazole has two N atoms on the opposite side of the molecule and cannot easily fulfil this requirement. Consequently, for imidazole, the cleavage of the C–H bond is thermodynamically preferred over the cleavage of the N–H bond on copper surfaces [82,85], but the barrier is considerably higher (in range from 0.6 to 0.9 eV) than for the cleavage of the N–H bond of triazoles [82,85] and mercaptoazoles [94]. Similar trends were also observed during the current calculations. In particular, imidazole's C2–H bond cleavage is usually preferred over the N1–H bond breaking, particularly on copper surfaces. As for mercaptobenzimidazoles, we observed that in some cases, the surface OH* groups induce molecular deprotonation during an adsorption relaxation calculation by forming the water molecule, i.e., MolH* + OH* → Mol* + H_2O*.

It is worth mentioning that only O- and OH-covered Cu(111) models are considered herein for copper surfaces, whereas the adsorption of Imd and MBI molecules on Cu_2O-based models was considered in our previous publications [2,42,82,83]. However, the current copper-based models are sufficient to capture the molecular adsorption characteristics qualitatively.

3.4.2. Adsorption structures and energies

To provide a better link with experiments, we currently address the adsorption of the azole compounds on ten different models of copper and zinc surfaces, described in Section 2.6 and Fig. 2, which are more relevant than bare metal surfaces in the context of corrosion. The reason for using different surface models is to try to account for surface heterogeneities and different surface chemistries.

We performed a thorough configurational search of potential adsorption structures of Imd, MBI, and MMBI molecules. In total, we considered 150 different adsorption structures, and here, we only present the most stable identified adsorption structures for each adsorption mode and surface model. The corresponding adsorption structures on O/Cu(111) and OH/Cu(111) are shown in Fig. 12 for molecular adsorption at low coverage of 1.1 molecule/nm^2 and in Fig. 13 for molecular adsorption at high coverage of 2.9 molecule/nm^2. Fig. 14 shows the molecular high coverage structures on O/Zn(001) and OH/Zn(001), and Fig. 15 shows the corresponding structures on hydroxylated ZnO(001). The adsorption Gibbs energies of these structures at the concentration of 1 mM and temperature of 298.15 K are presented in Tables 6 and 7. To help systemise these results, Fig. 16 schematically presents identified adsorption forms of the three molecules on Cu and Zn surfaces, and Fig. 17 presents the span of their adsorption Gibbs energies on the considered surface models.

Cu and Zn surfaces display different adsorption characteristics not only for azole molecules but also toward chemisorbed O* adatoms and OH* groups. According to our calculations, O* adatoms adsorb onto fcc sites on Cu(111) and hcp sites on Zn(001). In contrast, on Cu(111), the most stable adsorption sites for OH* are fcc at low coverage and bridge at high coverage, the latter being preferred due to the formation of hydrogen bonds between neighbouring OH* groups. On Zn(001), the most stable OH* adsorption site is the bridge, irrespective of the coverage. The utilised O- and OH-covered Cu(111) and Zn(001) models (Fig. 2) were built according to these adsorption preferences. It is further worth noting that bulk Zn is a much "softer" metal than Cu, i.e., it has a twice smaller bulk modulus (70 GPa) than Cu (140 Gpa) [95] and a much weaker cohesion energy: the calculated values are −1.24 eV/atom for hcp-Zn and −3.46 eV/atom for fcc-Cu. Therefore, it is not surprising that in adsorption calculations, we observed that Zn(001)-based models are quite deformable with a substantial adsorption-induced buckling of surface Zn atoms.

An important observation from Figs. 12–15 is that MBI and MMBI display analogous adsorption structures, with MMBI adsorbing slightly stronger than MBI; the average difference of tabulated adsorption Gibbs energy values in Tables 6 and 7 between the two compounds is 0.04 eV, which is not surprising because the methyl group of MMBI is not involved in adsorption bonding with the surface, and, therefore, should not have a significant effect on adsorption bonding.

According to adsorption Gibbs energy results of Tables 6 and 7, all

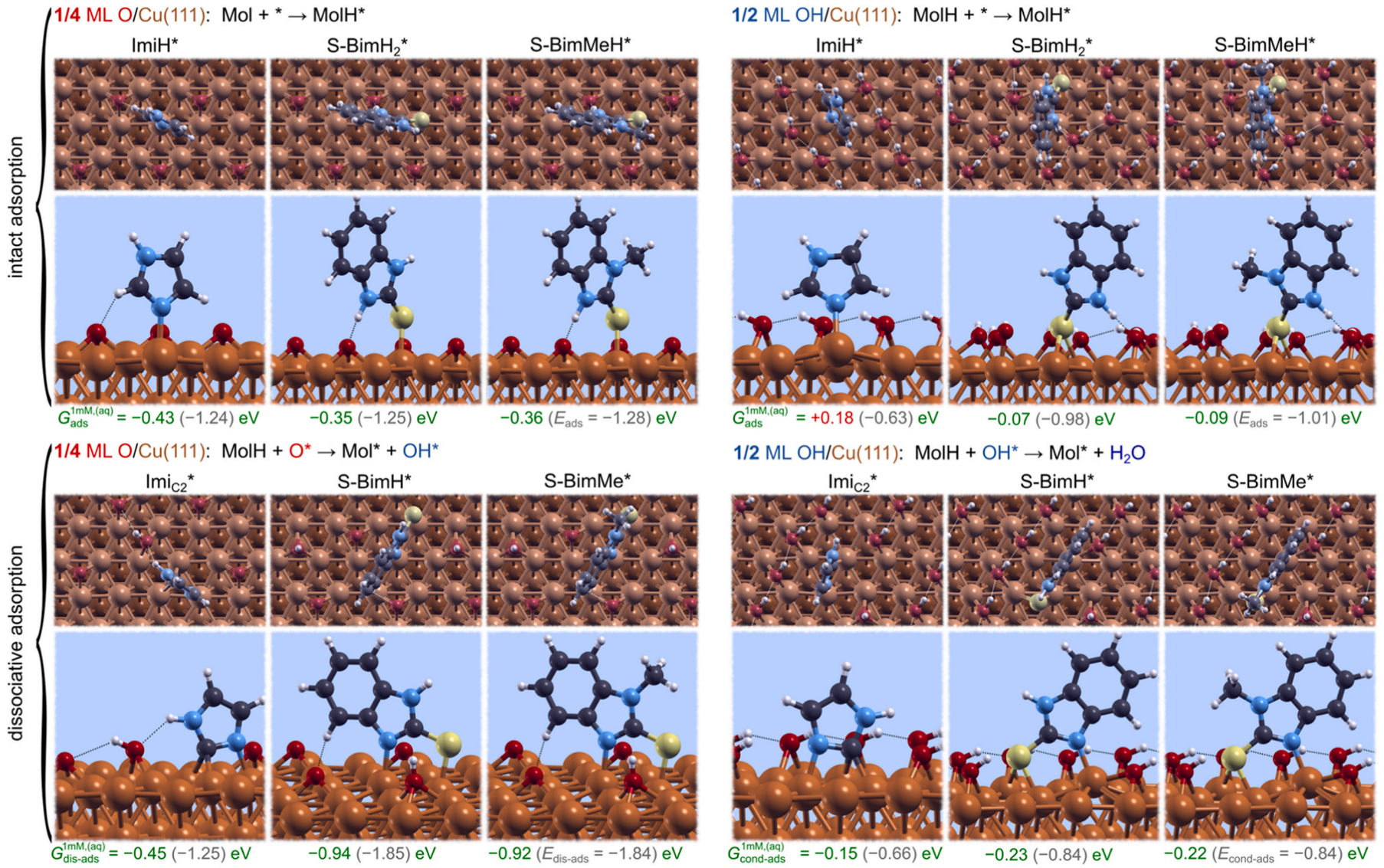

Fig. 12. Top-view and side-view snapshots of the most stable identified low-coverage adsorption structures of imidazole, 2-mercaptobenzimidazole, and 2-mercapto-1-methylbenzimidazole on the 1/4 ML O/Cu(111)–(4×4) (left) and 1/2 ML OH/Cu(111)–(4×4) (right) surface models. The intact adsorption structures are shown in the top row, whereas dissociatively adsorbed molecular structures are shown in the bottom row (for the latter, the coverage of O* and OH* refers to the coverage before adsorption). Adsorption Gibbs energies at $c = 1$ mM and $T = 298.15$ K (green numbers) and adsorption energies (grey numbers) are also stated.

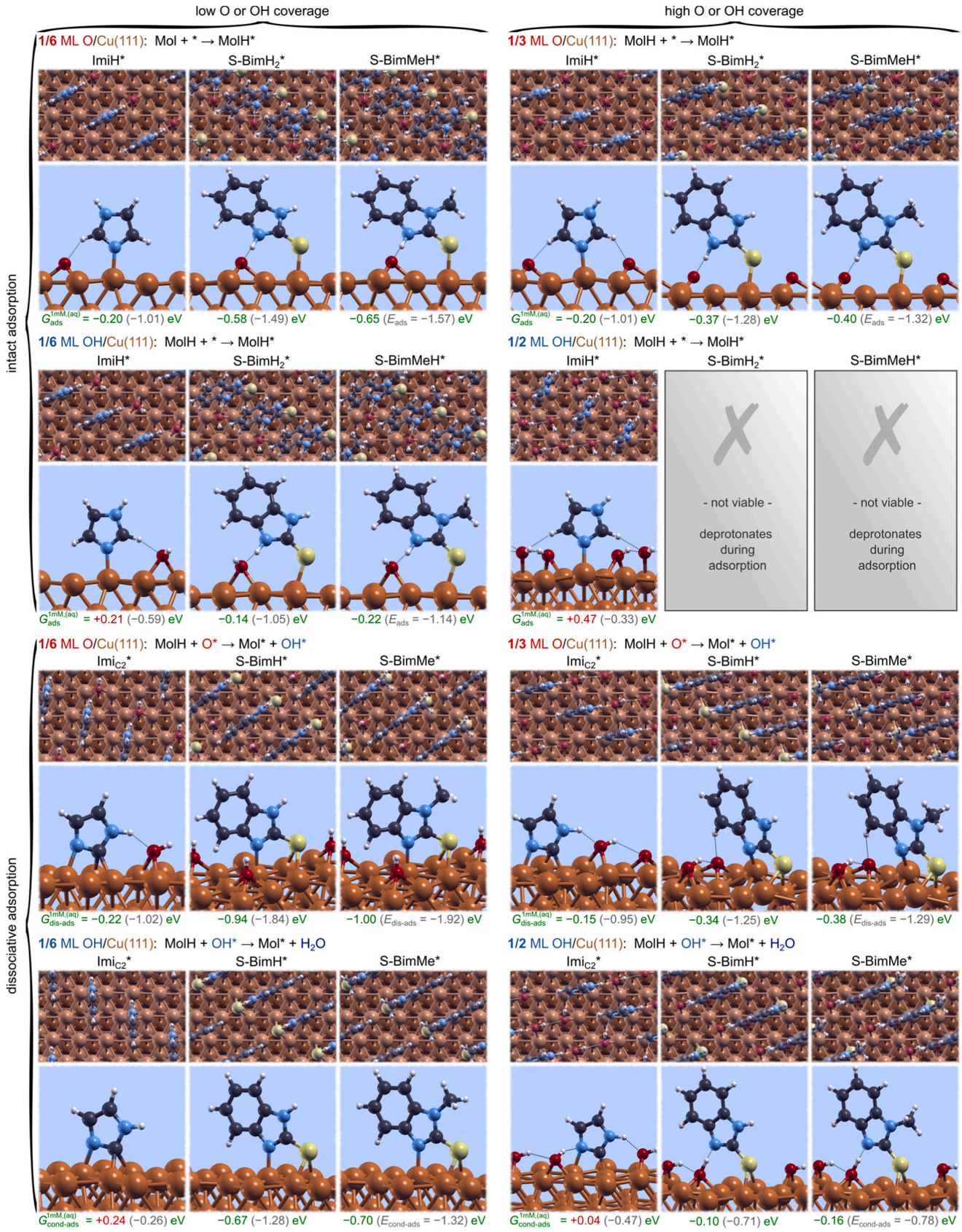

Fig. 13. Similar to Fig. 12 but for the high-coverage adsorption structures of imidazole, 2-mercaptobenzimidazole, and 2-mercapto-1-methylbenzimidazole on 1/6 ML O-covered, 1/3 ML O-covered, 1/6 ML OH-covered, and 1/2 ML OH-covered Cu(111)–$\begin{pmatrix} 4 & 2 \\ -1 & 1 \end{pmatrix}$. The intact adsorption structures are shown in the two top rows, whereas dissociatively adsorbed molecular structures are shown in the two bottom rows (for the latter, the coverage of O* and OH* refers to the coverage before adsorption). Adsorption Gibbs energies at $c = 1$ mM and $T = 298.15$ K (green numbers) and adsorption energies (grey numbers) are also stated.

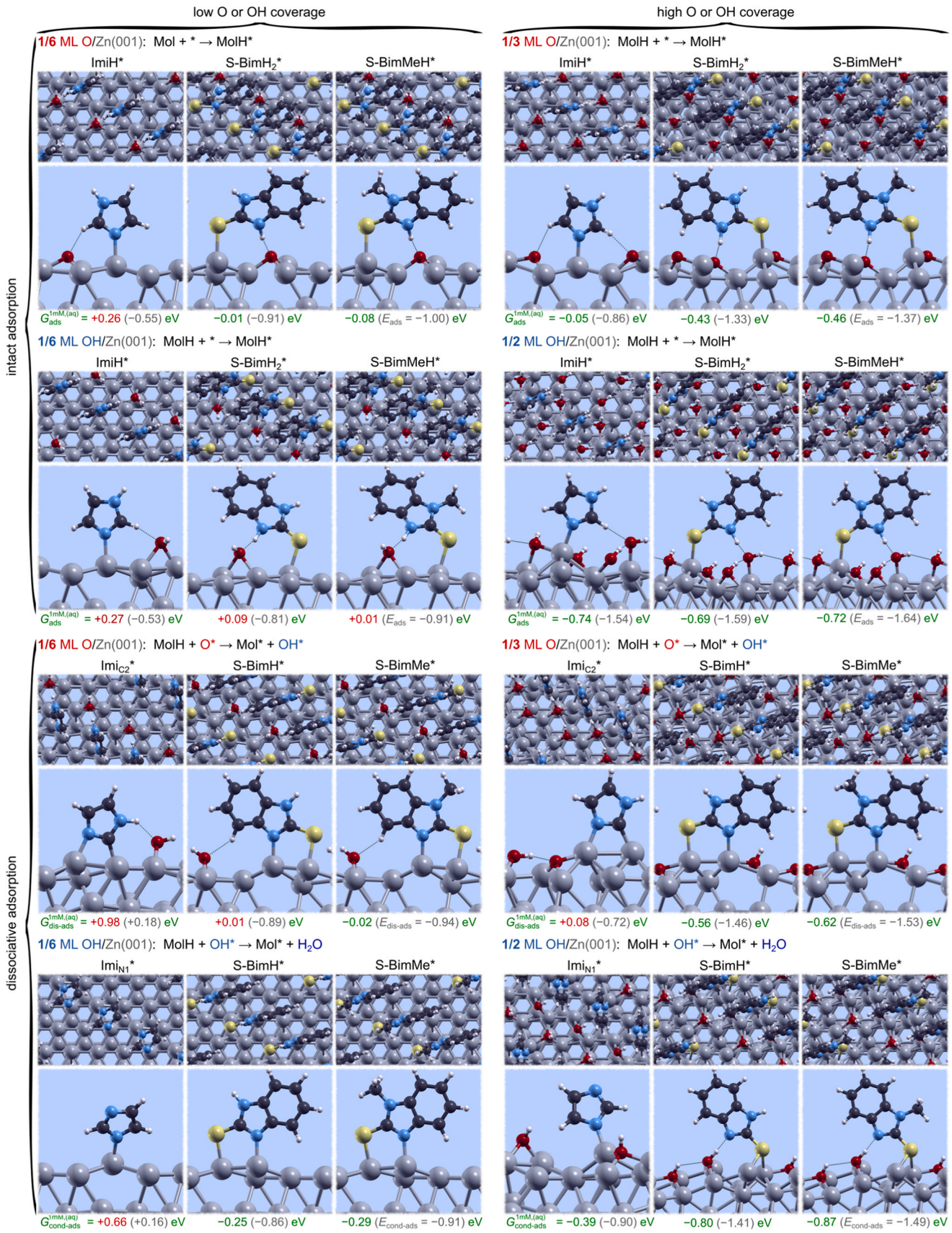

Fig. 14. Similar to Fig. 13 but for the high-coverage molecular adsorption structures on O- and OH-covered Zn(001)–$\begin{pmatrix} 4 & 2 \\ -1 & 1 \end{pmatrix}$ surfaces.

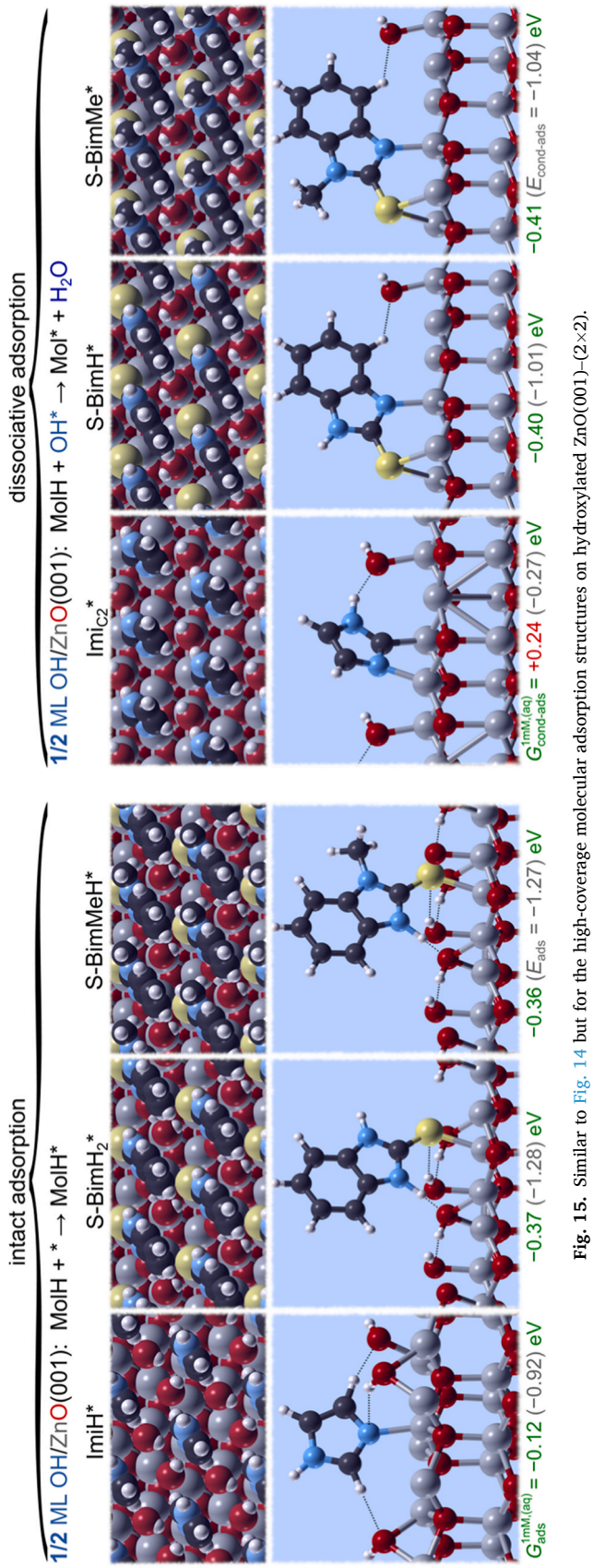

Fig. 15. Similar to Fig. 14 but for the high-coverage molecular adsorption structures on hydroxylated ZnO(001)–(2×2).

Table 6
Low-coverage adsorption Gibbs energies (at $c = 1$ mM and $T = 298.15$ K) estimated in aqueous phase with Eqs. (13), (14), and (15) for intact, dissociative, and dissociative-condensation adsorbed imidazole, 2-mercaptobenzimidazole, and 2-mercapto-1-methylbenzimidazole on O- and OH-covered Cu(111)–(4×4). The snapshots of the corresponding adsorption structures are shown in Fig. 12.

	Adsorption Gibbs energies (eV)	
	1/4 ML O @ Cu(111)–(4×4)	1/2 ML OH @ Cu(111)–(4×4)
imidazole		
ImiH + * → ImiH*	−0.43	+0.18
ImiH + O* → Imi* + OH*	−0.45	
ImiH + OH* → Imi* + H_2O		−0.15
2-mercaptobenzimidazole		
S-BimH_2 + * → S-BimH_2*	−0.35	−0.07
S-BimH_2 + O* → S-BimH* + OH*	−0.94	
S-BimH_2 + OH* → S-BimH* + H_2O		−0.23
2-mercapto-1-methylbenzimidazole		
S-BimMeH + * → S-BimMeH*	−0.36	−0.09
S-BimMeH + O* → S-BimMe* + OH*	−0.92	
S-BimMeH + OH* → S-BimMe* + H_2O		−0.22

three molecular compounds adsorb significantly more exergonic on O/Cu(111) than OH/Cu(111). For imidazole, intact ImiH and C2-deprotonated Imi (Imi_{C2}) display similar stability on O/Cu(111) with the adsorption Gibbs energy (at $c = 1$ mM and $T = 298.15$ K) of about −0.4 eV at low molecular coverage (Table 6) and −0.2 eV at high molecular coverage (Table 7). Intact adsorbed ImiH binds with its N3 atom to a single Cu atom and, moreover, usually forms the C–H···O hydrogen bond with the nearby O* or OH*. C2-deprotonated Imi binds with its C2 to two Cu atoms and with N3 to another Cu atom, and usually forms the N–H···O hydrogen bond with the nearby OH*. In contrast to imidazole, dissociative adsorption (including condensation adsorption) is more exergonic than intact adsorption for MBI and MMBI on copper surfaces, with the dissociative and condensation adsorption Gibbs energies (at $c = 1$ mM and $T = 298.15$ K) reaching the values of about −1.0 eV and −0.7 eV, respectively (Table 7). Two different forms of dissociatively adsorbed S-BimH and S-BimMe can be observed in Fig. 13, i.e., the molecules can adsorb by forming either the S–Cu and N–Cu chemical bonds or only the S–Cu chemical bond, with the N atom forming the N···HO hydrogen bond with the nearby OH* group. It is further worth noting that on bare Cu(111), the S atom of S-BimX (X = H_2, H, MeH, or Me) prefers to bond with two Cu atoms [24], but on O/Cu(111) and OH/Cu(111), the S atom can shift toward the top site to bond with only one Cu atom either due to the N–H···O hydrogen bond (thiones only), N···H–O hydrogen bond (thiolates only) or due to unavailability of a free bridge site due to nearby O* or OH* groups.

In contrast to Cu surfaces, where molecular adsorption on O-covered surfaces is more stable than on OH-covered surfaces, the vice versa is true on Zn surfaces. For imidazole, intact adsorption mode is significantly more stable than dissociative (including condensation) adsorption, and the most exergonic value of adsorption Gibbs energy (at $c = 1$ mM and $T = 298.15$ K) is about −0.7 eV (to be compared with about −0.2 eV on Cu surfaces). The intact adsorbed ImiH binds with the N3 atom to a single Zn atom and forms the C–H···O hydrogen bond with the nearby O* or OH*, whereas C2-deprotonated Imi binds with its C2 to a single Zn atom (in contrast, C2 binds to two Cu atoms on Cu surfaces) and with N3 to another Zn atom, and usually forms the N–H···O hydrogen bond with the nearby OH*. In contrast to imidazole, dissociative condensation adsorption is more exergonic than intact adsorption for MBI and MMBI on zinc surfaces, but there are also instances of significantly exergonic intact adsorption. In particular, the most exergonic values of adsorption Gibbs energy (at $c = 1$ mM and $T = 298.15$ K) are, for condensation adsorption, about −0.8 eV for MBI and −0.9 eV for MMBI and, for intact adsorption, about −0.7 eV for both molecules (Table 7). On Zn(001)-based surface models, the S atom of the MBI and

Table 7
High-coverage adsorption Gibbs energies (at c = 1 mM and T = 298.15 K) estimated in aqueous phase with Eqs. (13), (14), and (15) for intact, dissociative, and dissociative-condensation adsorbed imidazole, 2-mercaptobenzimidazole, and 2-mercapto-1-methylbenzimidazole on O- and OH-covered Cu(111)–$\begin{pmatrix} 4 & 2 \\ -1 & 1 \end{pmatrix}$ and Zn(001)–$\begin{pmatrix} 4 & 2 \\ -1 & 1 \end{pmatrix}$, and on hydroxylated ZnO(001)–(2×2). The snapshots of the corresponding adsorption structures are shown in Figs. 13–15.

	Adsorption Gibbs energies (eV)								
	O @ Cu(111)		OH @ Cu(111)		O @ Zn(001)		OH @ Zn(001)		OH @ ZnO(001)
Adsorption reaction O or OH coverage → ↓	1/6 ML	1/3 ML	1/6 ML	1/2 ML	1/6 ML	1/3 ML	1/6 ML	1/2 ML	1/2 ML
imidazole									
ImiH + * → ImiH*	−0.20	−0.20	+0.21	+0.47	+0.26	−0.05	+0.27	−0.74	−0.12
ImiH + O* → Imi* + OH*	−0.22	−0.15			+0.98	+0.08			
ImiH + OH* → Imi* + H_2O			+0.24	+0.04			+0.66	−0.39	+0.24
2-mercaptobenzimidazole									
S-BimH_2 + * → S-BimH_2*	−0.58	−0.37	−0.14	n/a[a]	−0.01	−0.43	+0.09	−0.69	−0.37
S-BimH_2 + O* → S-BimH* + OH*	−0.94	−0.34			+0.01	−0.56			
S-BimH_2 + OH* → S-BimH* + H_2O			−0.67	−0.10			−0.25	−0.80	−0.40
2-mercapto-1-methylbenzimidazole									
S-BimMeH + * → S-BimMeH*	−0.65	−0.40	−0.22	n/a[a]	−0.08	−0.46	+0.01	−0.72	−0.36
S-BimMeH + O* → S-BimMe* + OH*	−1.00	−0.38			−0.02	−0.62			
S-BimMeH + OH* → S-BimMe* + H_2O			−0.70	−0.16			−0.29	−0.87	−0.41

[a] Does not exist because it dissociates without barrier as MolH + OH* → Mol* + H_2O*.

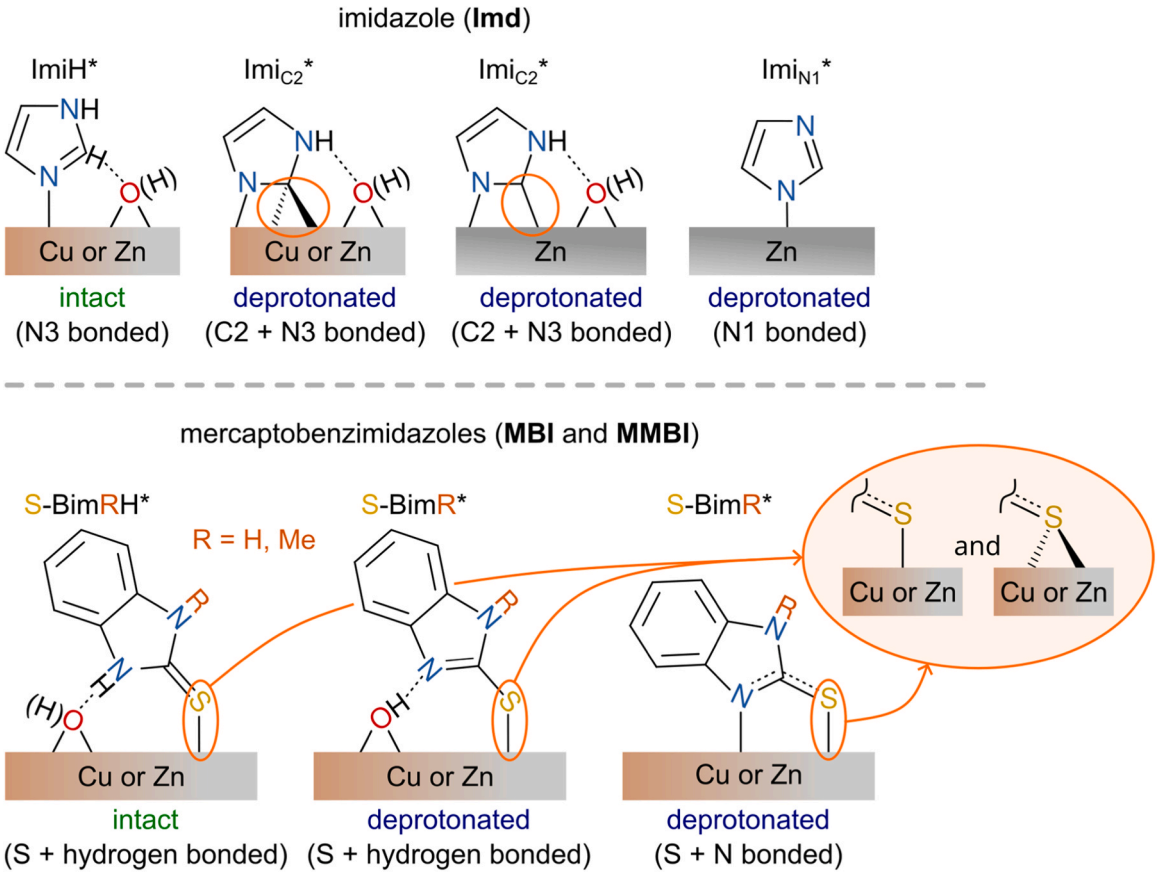

Fig. 16. A simplified skeletal representation of identified adsorption modes of Imd (top row) and MBI and MMBI (bottom row) on Cu and Zn surfaces. The label "Cu or Zn" indicates that the corresponding adsorption structure was identified on both metal substrates, while the label "O(H)" indicates both O and OH. For mercapto molecules, S can bond to either a single metal atom or two metal atoms, as indicated in the inset.

MMBI compounds prefer to bond with a single Zn atom for both thiones and thiolates. In contrast, on hydroxylated ZnO(001), the S atom bonds with two surface Zn ions. Similarly to Cu surfaces, also on Zn surfaces, two different forms of dissociatively adsorbed S-BimH and S-BimMe can be observed in Fig. 14, i.e., the molecules can adsorb by forming either the S–Zn and N–Zn chemical bonds or only the S–Zn chemical bond, with the N atom forming the N···HO hydrogen bond with the nearby OH* group. To help memorise various adsorption modes of Imd, MBI, and MMBI molecules on Cu and Zn surfaces, Fig. 16 presents skeletal representations of the molecular adsorption structures described above.

To systemise a relatively large set of adsorption Gibbs energies of Tables 6 and 7, Fig. 17 presents them graphically. This figure reveals

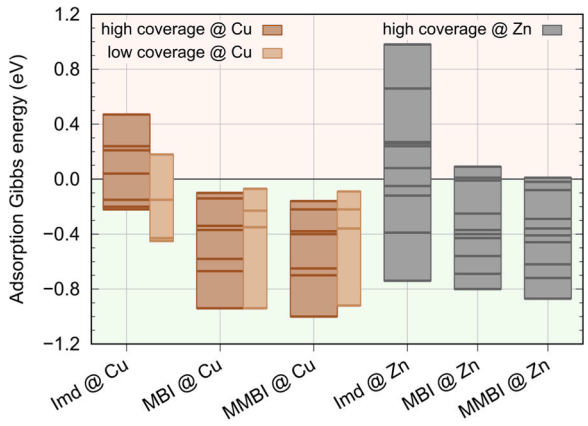

Fig. 17. The aqueous-phase adsorption Gibbs energies (at $c = 1$ mM and $T = 298.15$ K) for the studied adsorption modes of imidazole (Imd), 2-mercaptobenzimidazole (MBI), and 2-mercapto-1-methylbenzimidazole (MMBI) on the models of Cu and Zn surfaces, presented in Fig. 2. Here, the adsorption Gibbs energies of adsorption structures shown in Figs. 12–15 are considered; individual adsorption Gibbs energy values are shown by horizontal lines, whereas the span from the minimum to maximum value of a given molecule on a given material is shown by rectangular bars.

that the adsorption of MBI and MMBI is more exergonic than that of imidazole. Broadly speaking, the adsorption Gibbs energies range from about 0 to −1 eV for MBI and MMBI on Cu and Zn surfaces, suggesting that these molecules display high adsorption affinity. In contrast, the adsorption Gibbs energies for imidazole straddle the zero value, suggesting that its adsorption affinity depends on surface details. While the adsorption Gibbs energies on Cu surfaces range from +0.5 to −0.4 eV, the corresponding range on Zn surfaces is from +1.0 eV to −0.7 eV. Therefore, the range of values is much broader on Zn surfaces, where adsorption also reaches more exergonic values. By cherry-picking these results, the lack of experimental detection of imidazole on Cu surfaces and the experimental observation of imidazole on Zn surfaces can be explained by assuming that under experimental conditions, the chemistry of Cu surfaces is compatible with the current models, which give endergonic adsorption Gibbs energies, and vice versa for the Zn surfaces.

An important insight provided by current calculations is that adsorption energies strongly depend on the surface model. For a given molecule on a given metal, the calculated adsorption (Gibbs) energies can vary within ranges as wide as 1 eV. This observation implies that one should be careful with the interpretation when adsorption calculations are performed only on a single surface model due to the surface heterogeneity of the samples used in experiments and because their atomic surface structure is rarely (if ever) known.

4. Conclusions

The action of organic Imd, MBI, and MMBI compounds as corrosion inhibitors for Cu, Cu-*x*Zn, and Zn samples was studied. The aim of this work was threefold. In the first part, electrochemical measurements were conducted in 3 wt% NaCl with and without adding 1 mM Imd, MBI, and MMBI to determine the long-term corrosion inhibition efficiency and mechanism of inhibition as a function of the type of organic compound and type of substrate. In the second part, surface analysis of the samples immersed in NaCl with and without adding Imd, MBI, and MMBI was carried out to reveal the surface composition, elemental speciation, and bonding types. In the third part, various adsorption modes of organic molecules were calculated for different surface models of Cu and Zn surfaces.

i. Linear polarisation resistance measurements conducted for 100 h revealed that MBI and MMBI are efficient corrosion inhibitors for Cu, Cu-*x*Zn alloys, and Zn, whereas Imd is less efficient. Potentiodynamic polarisation curves confirmed the LPR results regarding efficiency and provided insight into the mechanisms: all three compounds acted as mixed inhibitors with a stronger inhibitory action on the anodic reaction, i.e., Cu and Zn dissolution. Polarisation curves of the Cu-*x*Zn alloys generally resemble more Cu than Zn, as reported previously but with increasing Zn content, the resemblance to the Zn curve became evident. When adding MBI and MMBI, forming organic inhibitor layers reduced anodic current density by several orders of magnitude. The layers formed by adding Imd were less efficient in terms of corrosion protection, especially for Cu and Cu-10Zn. Imd was fairly efficient on Cu-40Zn and Zn; however, on Zn, the effect faded after a prolonged immersion of 30 h. In contrast, the degree of inhibition assured by MBI and MMBI even improved by prolonged immersion.

ii. Based on the FTIR and XPS analyses, it can be stated that the immersion of Cu, Zn, and Cu-*x*Zn samples results in the formation of the inhibitor-containing layer at the surface. FTIR can recognise some organic functional groups more readily than XPS, i.e., C═N and C−N bonds, phenyl ring, and C═S bond in layers formed by MBI and MMBI. XPS confirmed the presence of C═N and C−N and showed that the ratio between these peaks changes for different inhibitors (predominantly C═N for Imd, and both C═N and C−N for MBI and MMBI with the prevalence of the latter in MMBI). The presence of the C−S bond was difficult to prove by both FTIR and XPS. The formation of the imidazole-containing layer was ambiguous by FTIR but clear by XPS. It was further shown by XPS that the imidazole-based layer is more abundant on Zn and Cu-40Zn than on Cu and Cu-10Zn. This finding may be related to the increased stability of ZnO at pH 8.3 in the presence of imidazole. In contrast, the layers of mercapto-based inhibitors seem to be similar regardless of the substrate.

iii. Using DFT calculations, a thorough configurational search of potential adsorption structures of Imd, MBI, and MMBI molecules was performed on several different models of copper and zinc surfaces. An important insight provided by current calculations is that adsorption energies strongly depend on the surface model. For a given molecule on a given metal, the calculated adsorption (Gibbs) energies can vary within ranges as broad as 1 eV. This observation implies that one should be careful with the interpretation when adsorption calculations are performed only on a single surface model due to the surface heterogeneity of the samples used in experiments and because their atomic surface structure is rarely (if ever) known.

iv. DFT calculations reveal that chemisorbed O atoms and surface hydroxyls groups promote molecular deprotonation upon adsorption, particularly for MBI and MMBI, for which deprotonated adsorption modes (i.e., thiolates) are more stable than intact adsorbed thiones. However, in some cases, also intact thiones adsorb strongly. In contrast, for imidazole, the deprotonated adsorption is either inferior (for Zn) or, at most, comparable in stability to the intact adsorption (on Cu). While on Cu surfaces, the C2-deprotonated imidazole is thermodynamically superior to the N1-deprotonated imidazole and of similar stability as the intact imidazole, the opposite is true on Zn surfaces (i.e., the intact imidazole is superior to the deprotonated one, and N1-deprotonated is more stable than C2-deprotonated).

v. The adsorption of MBI and MMBI is, in general, more exergonic than that of imidazole, with the calculated adsorption Gibbs energies (at room temperature and 1 mM concentration) ranging from about 0 to −1 eV, suggesting that these molecules display high adsorption affinity. In contrast, the values for imidazole straddle the zero value, implying that its adsorption affinity depends on surface details. The calculated adsorption Gibbs energies of imidazole can reach more exergonic values on Zn than

Cu surfaces, which seems in agreement with spectroscopic experiments that detected imidazole on Zn samples, while its presence on Cu samples was not unambiguous proved.

Author statement

All persons who meet authorship criteria are listed as authors, and all authors certify that they have participated sufficiently in the work to take public responsibility for the content, including participation in the concept, design, analysis, writing, or revision of the manuscript. The authors declare that the science contained in this manuscript has not been previously published and is not under consideration by any other journal.

Funding

This work is a part of the M-ERA.NET project entitled "*Corrosion inhibition and dealloying descriptors*" (acronym COIN DESC). The financial support of the project by MESS (Ministry of Education, Science and Sport of the Republic of Slovenia) and NWO (Netherlands Organisation for Scientific Research) is acknowledged. The authors also acknowledge the financial support of the Slovenian Research and Innovation Agency (research core funding No. P2-0393).

CRediT authorship contribution statement

Barbara Kapun: Formal analysis. **Dževad K Kozlica:** Writing – original draft, Formal analysis. **Arjan Mol:** Writing – review & editing, Writing – original draft, Methodology, Conceptualization. **Ingrid Milošev:** Writing – review & editing, Writing – original draft, Investigation, Formal analysis, Conceptualization. **Peyman Taheri:** Writing – review & editing, Writing – original draft, Methodology, Formal analysis, Conceptualization. **Anton Kokalj:** Writing – review & editing, Writing – original draft, Supervision, Methodology, Funding acquisition, Formal analysis, Conceptualization.

Declaration of Competing Interest

The author declare that they have no known competing financial interests or personal relationships that could have appeared to influence the work reported in this paper.

Data availability

Data will be made available on request.

Acknowledgements

The authors acknowledge the funding agencies (see the Funding section). Wieland-Werke AG, Ulm, Germany, is acknowledged for supplying the Cu-*x*Zn samples. The authors thank Prof. Janez Kovač and Tatjana Filipič, MSc, the Department of Surface Engineering, for the acquisition of XPS spectra and Dr. Urša Tiringer of the Department of Physical and Organic Chemistry for her help in the spectra presentation.

Appendix A. Supporting information

Supplementary data associated with this article can be found in the online version at doi:10.1016/j.corsci.2024.112328.

References

[1] T.H. Muster, A.E. Hughes, S.A. Furman, T. Harvey, N. Sherman, S. Hardin, P. Corrigan, D. Lau, F.H. Scholes, P.A. White, M. Glenn, J. Mardel, S.J. Garcia, J.M. C. Mol, A rapid screening multi-electrode method for the evaluation of corrosion inhibitors, Electrochim. Acta 54 (2009) 3402–3411.

[2] D.K. Kozlica, A. Kokalj, I. Milošev, Synergistic effect of 2-mercaptobenzimidazole and octylphosphonic acid as corrosion inhibitors for copper and aluminium – An electrochemical, XPS, FTIR and DFT study, Corros. Sci. 182 (2021) 109082, https://doi.org/10.1016/j.corsci.2020.109082.

[3] S.J. Garćia, T.H. Muster, Ö. Özkanat, N. Sherman, A.E. Hughes, H. Terryn, J.H. W. de Wit, J.M.C. Mol, The influence of pH on corrosion inhibitor selection for 2024-T3 aluminium alloy assessed by high-throughput multielectrode and potentiodynamic testing, Electrochim. Acta 55 (2010) 2457–2465.

[4] A. Kokalj, Molecular modeling of organic corrosion inhibitors: calculations, pitfalls, and conceptualisation of molecule–surface bonding, Corros. Sci. 193 (2021) 109650.

[5] A. Kokalj, D. Costa, Molecular modelling of corrosion inhibitors, in: in: Reference Module in Chemistry, Molecular Sciences and Chemical Engineering, 61, Elsevier, 2018, pp. 332–345.

[6] A. Kokalj, *Ab initio* modeling of the bonding of benzotriazole corrosion inhibitor to reduced and oxidized copper surfaces, Faraday Discuss. 180 (2015) 415–438.

[7] D.A. Winkler, Predicting the performance of organic corrosion inhibitors, Metals 7 (2017) 553.

[8] C.D. Taylor, A. Chandra, J. Vera, N. Sridhar, A multiphysics perspective on mechanistic models for chemical corrosion inhibitor performance, J. Electrochem. Soc. 162 (7) (2015) C369–C375.

[9] C. Monticelli, Corrosion inhibitors, in: in: Reference Module in Chemistry, Molecular Sciences and Chemical Engineering, 61, Elsevier, 2018, pp. 164–171.

[10] Y.I. Kuznetsov, L.P. Kazansky, Physicochemical aspects of metal protection by azoles as corrosion inhibitors, Russ. Chem. Rev. 77 (3) (2008) 219–232.

[11] M.M. Antonijevic, M.B. Petrovic, Copper corrosion inhibitors. A review, Int. J. Electrochem. Sci. 3 (2008) 1–28.

[12] M. Finšgar, I. Milošev, Inhibition of copper corrosion by 1,2,3-benzotriazole: a review, Corros. Sci. 52 (2010) 2737–2749.

[13] A. Kokalj, S. Peljhan, M. Finšgar, I. Milošev, What determines the inhibition effectiveness of ATA, BTAH, and BTAOH corrosion inhibitors on copper? J. Am. Chem. Soc. 132 (2010) 16657–16668.

[14] M. Finšgar, A. Lesar, A. Kokalj, I. Milošev, A comparative electrochemical and quantum chemical calculation study of BTAH and BTAOH as corrosion inhibitors in near neutral chloride solution, Electrochim. Acta 53 (2008) 8287–8297.

[15] A. Lesar, I. Milošev, Density functional study of the corrosion inhibition properties of 1,2,4-triazole and its amino derivatives, Chem. Phys. Lett. 483 (2009) 198–203.

[16] A. Kokalj, N. Kovačević, S. Peljhan, M. Finšgar, A. Lesar, I. Milošev, Triazole, benzotriazole, and naphtotriazole as copper corrosion inhibitors: I. Molecular electronic and adsorption properties, ChemPhysChem 12 (2011) 3547–3555.

[17] R. Walker, Triazole, benzotriazole and naphthotriazole as corrosion inhibitors for copper, Corrosion 31 (1975) 97–100.

[18] I. Milošev, Contemporary modes of corrosion protection and functionalization of materials, Acta Chim. Slov. 66 (2019) 511–533.

[19] I. Milošev, N. Kovačević, J. Kovač, A. Kokalj, The roles of mercapto, benzene and methyl groups in the corrosion inhibition of imidazoles on copper: I. Experimental characterization, Corros. Sci. 98 (2015) 107–118.

[20] N. Kovačević, I. Milošev, A. Kokalj, How relevant is the adsorption bonding of imidazoles and triazoles for their inhibition of copper? Corros. Sci. 124 (2017) 25–34.

[21] A. Kokalj, M. Lozinšek, B. Kapun, P. Taheri, S. Neupane, P. Losada Pérez, C. Xie, S. Stavber, D. Crespo, F.U. Renner, A. Mol, I. Milošev, Simplistic correlations between molecular electronic properties and inhibition efficiences: do they really exist? Corros. Sci. 179 (2021) 108856 https://doi.org/10.1016/j.corsci.2020.108856.

[22] S. Neupane, P. Losada-Pérez, U. Tiringer, P. Taheri, D. Desta, C. Xie, D. Crespo, A. Mol, I. Milošev, A. Kokalj, F.U. Renner, Study of mercaptobenzimidazoles as inhibitors for copper corrosion: down to the molecular scale, J. Electrochem. Soc. 168 (2021) 051504, https://doi.org/10.1149/1945-7111/abf9c3.

[23] P. Taheri, I. Milošev, M. Meeusen, B. Kapun, P. White, A. Kokalj, A. Mol, On the importance of time-resolved electrochemical evaluation in corrosion inhibitor-screening studies, npj Mater. Degrad., 4 (2029) 12. https://doi.org/10.1038/s41529-020-0116-z.

[24] N. Kovačević, I. Milošev, A. Kokalj, The roles of mercapto, benzene and methyl groups in the corrosion inhibition of imidazoles on copper: II. Inhibitor-copper bonding, Corros. Sci. 98 (2015) 457–470.

[25] I. Milošev, N. Kovačević, A. Kokalj, Effect of mercapto and methyl groups on the efficiency of imidazole and benzimidazole-based inhibitors of iron corrosion, Acta Chim. Slov. 63 (2016) 544–559.

[26] A. Kokalj, Is the analysis of molecular electronic structure of corrosion inhibitors sufficient to predict the trend of their inhibition performance, Electrochim. Acta 56 (2010) 745–755.

[27] D. Chadwick, T. Hashemi, Electron spectroscopy of corrosion inhibitors: surface films formed by 2-mercaptobenzothiazole and 2-mercaptobenzimidazole on copper, Surf. Sci. 89 (1979) 649–659.

[28] G. Xue, X.-Y. Huang, J. Dong, J. Zhang, The formation of an effective anti-corrosion film on copper surfaces from 2-mercaptobenzimidazole solution, J. Electroanal. Chem. 310 (1991) 139–148.

[29] M.G. Hosseini, H. Tavakoli, T. Shahrabi, Synergism in copper corrosion inhibition by sodium dodecylbenzenesulphonate and 2-mercaptobenzimidazole, J. Appl. Electrochem 38 (2008) 1629–1636.

[30] J. Izquierdo, J.J. Santana, S. Gonzáles, R.M. Souto, Scanning microelectrochemical characterization of the anti-corrosion performance of inhibitor films formed by 2-mercaptobenzimidazole on copper, Prog. Org. Coat. 74 (2012) 526–533.

[31] M. Finšgar, 2-mercaptobenzimidazole as a copper corrosion inhibitor: Part I. Long-term immersion, 3-D profilometry, and electrochemistry, Corros. Sci. 72 (2013) 82–89.

[32] M. Finšgar, 2-mercaptobenzimidazole as a copper corrosion inhibitor: Part II. Surface analysis using X-ray photoelectron spectroscopy, Corros. Sci. 72 (2013) 90–98.

[33] X. Wu, F. Wiame, V. Maurice, P. Marcus, 2-mercaptobenzimidazole films formed at ultra-low pressure on copper: adsorption, thermal stability and corrosion inhibition performance, Appl. Surf. Sci. 527 (2020) 146814.

[34] T. Kosec, I. Milošev, B. Pihlar, Benzotriazole as an inhibitor of brass corrosion in chloride solution, Appl. Surf. Sci. 253 (2007) 8863–8873.

[35] E. Kretschmann, H. Raether, Radiative decay of non-radiative surface plasmons excited by light, Z. Naturforsch. 23 A (1968) 2135–2136.

[36] J.H. Scofield, Hartree-Slater subshell photoionization cross-sections at 1254 and 1487 eV, J. Electron Spectrosc. Relat. Phenom. 8 (1976) 129–137.

[37] R.F. Reilman, A. Msezane, S.T. Manson, Relative intensities in photoelectron spectroscopy of atoms and molecules, J. Electron Spectrosc. Relat. Phenom. 8 (1976) 389–394.

[38] J.P. Perdew, K. Burke, M. Ernzerhof, Generalized gradient approximation made simple, Phys. Rev. Lett. 77 (1996) 3865–3868, https://doi.org/10.1103/PhysRevLett.77.3865.

[39] S. Grimme, Semiempirical GGA-type density functional constructed with a long-range dispersion correction, J. Comput. Chem. 27 (2006) 1787–1799.

[40] P. Giannozzi, S. Baroni, N. Bonini, M. Calandra, R. Car, C. Cavazzoni, D. Ceresoli, G.L. Chiarotti, M. Cococcioni, I. Dabo, A. Dal Corso, S. de Gironcoli, S. Fabris, G. Fratesi, R. Gebauer, U. Gerstmann, C. Gougoussis, A. Kokalj, M. Lazzeri, L. Martin-Samos, N. Marzari, F. Mauri, R. Mazzarello, S. Paolini, A. Pasquarello, L. Paulatto, C. Sbraccia, S. Scandolo, G. Sclauzero, A.P. Seitsonen, A. Smogunov, P. Umari, R.M. Wentzcovitch, QUANTUM ESPRESSO: a modular and open-source software project for quantum simulations of materials, J. Phys. Condens. Matter 21 (2009) 395502.

[41] P. Giannozzi, O. Andreussi, T. Brumme, O. Bunau, M.B. Nardelli, M. Calandra, R. Car, C. Cavazzoni, D. Ceresoli, M. Cococcioni, N. Colonna, I. Carnimeo, A. D. Corso, S. de Gironcoli, P. Delugas, R.A.D. Jr, A. Ferretti, A. Floris, G. Fratesi, G. Fugallo, R. Gebauer, U. Gerstmann, F. Giustino, T. Gorni, J. Jia, M. Kawamura, H.-Y. Ko, A. Kokalj, E. Küçükbenli, M. Lazzeri, M. Marsili, N. Marzari, F. Mauri, N. L. Nguyen, H.-V. Nguyen, A. Otero-de-la-Roza, L. Paulatto, S. Poncé, D. Rocca, R. Sabatini, B. Santra, M. Schlipf, A.P. Seitsonen, A. Smogunov, I. Timrov, T. Thonhauser, P. Umari, N. Vast, X. Wu, S. Baroni, Advanced capabilities for materials modelling with Quantum ESPRESSO, J. Phys. Condens. Matter 29 (2017) 465901, https://doi.org/10.1088/1361-648X/aa8f79.

[42] D. Gustinčič, A. Kokalj, A DFT study of adsorption of imidazole, triazole, and tetrazole on oxidized copper surfaces: $Cu_2O(111)$ and $Cu_2O(111)$-w/o-Cu^{CUS}, Phys. Chem. Chem. Phys. 17 (2015) 28602–28615, https://doi.org/10.1039/C5CP03647J.

[43] E.R. McNellis, J. Meyer, K. Reuter, Azobenzene at coinage metal surfaces: role of dispersive van der Waals interactions, Phys. Rev. B 80 (2009) 205414, https://doi.org/10.1103/PhysRevB.80.205414.

[44] K. Tonigold, A. Groß, Adsorption of small aromatic molecules on the (111) surfaces of noble metals: a density functional theory study with semiempirical corrections for dispersion effects, J. Chem. Phys. 132 (2010) 224701, https://doi.org/10.1063/1.3439691.

[45] A. Kokalj, S. Peljhan, Density functional theory study of ATA, BTAH, and BTAOH as copper corrosion inhibitors: adsorption onto Cu(111) from gas phase, Langmuir 26 (2010) 14582–14593, https://doi.org/10.1021/la1019789.

[46] D. Vanderbilt, Soft self-consistent pseudopotentials in a generalized eigenvalue formalism, Phys. Rev. B 41 (1990) 7892–7895.

[47] Ultrasoft pseudopotentials for H, C, N, O, S, Cu and Zn atoms were taken from the Quantum Espresso Pseudopotential Download Page, ⟨https://www.quantum-espresso.org/pseudopotentials⟩. Files: H.pbe-rrkjus.UPF, C.pbe-rrkjus.UPF, N.pbe-rrkjus.UPF, O.pbe-rrkjus.UPF, S.pbe-van_bm.UPF, Cu.pbe-d-rrkjus.UPF, and Zn.pbe-van.UPF.

[48] P.W. Tasker, The stability of ionic crystal surfaces, J. Phys. C: Solid State Phys. 12 (1979) 4977, https://doi.org/10.1088/0022-3719/12/22/036.

[49] M. Cococcioni, S. de Gironcoli, Linear response approach to the calculation of the effective interaction parameters in the LDA+U method, Phys. Rev. B 71 (2005) 035105, https://doi.org/10.1103/PhysRevB.71.035105.

[50] M. Methfessel, A.T. Paxton, High-precision sampling for Brillouin-zone integration in metals, Phys. Rev. B 40 (1989) 3616–3621, https://doi.org/10.1103/PhysRevB.40.3616.

[51] O. Andreussi, N. Marzari, Electrostatics of solvated systems in periodic boundary conditions, Phys. Rev. B 90 (2014) 245101, https://doi.org/10.1103/PhysRevB.90.245101.

[52] O. Andreussi, I. Dabo, N. Marzari, Revised self-consistent continuum solvation in electronic-structure calculations, J. Chem. Phys. 136 (2012) 064102, https://doi.org/10.1063/1.3676407.

[53] A. Kokalj, XCrySDen–a new program for displaying crystalline structures and electron densities, J. Mol. Graph. Model 17 (1999) 176–179.

[54] A. Kokalj, Corrosion inhibitors: physisorbed or chemisorbed? Corros. Sci. 196 (2022) 109939 https://doi.org/10.1016/j.corsci.2021.109939.

[55] M. Poberžnik, F. Chiter, I. Milošev, P. Marcus, D. Costa, A. Kokalj, DFT study of *n*-alkyl carboxylic acids on oxidized aluminum surfaces: from standalone molecules to self-assembled-monolayers, Appl. Surf. Sci. 525 (2020) 146156, https://doi.org/10.1016/j.apsusc.2020.146156.

[56] D.J. Gardiner, A.C. Gorvin, C. Gutteridge, A.R. Jackson, E.S. Raper, In situ characterization of corrosion inhibition complexes on copper surfaces using raman microscopy, Corros. Sci. 25 (1985) 1019–1027.

[57] C. Deslouis, B. Tribollet, G. Mengoli, M. Musiani, Electrochemical behaviour of copper in neutral aerated chloride solution. I. Steady-state investigation, J. Appl. Electrochem. 18 (1988) 374–383.

[58] S. Thomas, N. Birbilis, M.S. Venkatraman, I.S. Cole, Corrosion of zinc as a function of pH, Corrosion 68 (2012), 015009-1-9.

[59] H.J. Flitt, D.P. Schweinsberg, Synthesis, matching and deconstruction of polarization curves for the active corrosion of zinc in aerated near-neutral solution, Corros. Sci. 52 (2010) 1905–1914.

[60] Y. Meng, L. Liu, D. Zhang, C. Dong, Y. Yan, A.A. Volinsky, L.-N. Wang, Initial formation of corrosion products on pure zinc in saline solution, Bioact. Mater. 4 (2019) 87–96.

[61] A. Sahai, N. Goswami, S.D. Kaushik, S. Tripathi, Cu/Cu_2O/CuO nanoparticles: novel synthesis by exploding wire technique and extensive characterization, Appl. Surf. Sci. 390 (2016) 974–983.

[62] B. Lefez, R. Souchet, K. Kartouni, M. Lenglet, Infrared reflection study of CuO in thin oxide films, Thin Solid Films 268 (1-2) (1995) 45–48.

[63] G. Di Carlo, C. Giuliani, C. Riccucci, M. Pascucci, E. Messina, G. Fierro, M. Lavorgna, G.M. Ingo, Artificial patina formation onto copper-based alloys: chloride and sulphate induced corrosion processes, Appl. Surf. Sci. 421 (2017) 120–127.

[64] C. Engelbrekt, P. Malcho, J. Andersen, L. Zhang, K. Ståhl, B. Li, J. Hu, J. Zhang, Selective synthesis of clinoatacamite $Cu_2(OH)_3Cl$ and tenorite CuO nanoparticles by pH control, J. Nanopart. Res. 16 (8) (2014) 2562.

[65] J. Coates, Interpretation of infrared spectra, a practical approach, Encycl. Anal. Chem. (2006), https://doi.org/10.1002/9780470027318.a5606.

[66] Z. Chen, L. Huang, G. Zhang, Y. Qiu, X. Guo, X, Benzotriazole as a volatile corrosion inhibitor during the early stage of copper corrosion under adsorbed thin electrolyte layers, Corros. Sci. 65 (2012) (2012) 214–222.

[67] R. Gleiter, E. Pretsch, T. Clerc, J. Seibl, W. Simon, Tabellen zur Strukturaufklärung organischer Verbindungen mit spektroskopischen Methoden, Springer Verlag, Berlin-Heildeberg-New York, 1976.

[68] V. Sathyanarayanmoorthi, R. Karunathan, V. Kannappan, Molecular modeling and spectroscopic studies of benzothiazole, J. Chem. 13 (2013) 258519, https://doi.org/10.1155/2013/258519.

[69] G. Socrates, Infrared and Raman Characteristic Group Frequencies: Tables and Charts, John Wiley & Sons, 2004.

[70] G. Xue, X. Huang, J. Ding, Surface reaction of 2-mercaptobenzimidazole on metals and its application in adhesion promotion, J. Chem. Soc. Faraday Trans. 87 (8) (1991) 1229–1232.

[71] IR Spectrum Table & Chart, technical document, Sigma Aldrich. ⟨https://www.sigmaaldrich.com/technical-documents/articles/biology/ir-spectrum-table.html⟩.

[72] N.S. Rao, M.B. Rao, Structural and optical investigation of ZnO nanopowders synthesized from zinc chloride and zinc nitrate, Am. J. Mater. Sci. *5* (3) (2015) 66–68.

[73] S. Suresh, K. Jayamoorthy, P. Saravanan, S. Karthikeyan, Switch-Off fluorescence of 5-amino-2-mercapto benzimidazole with Ag_3O_4 nanoparticles: experimental and theoretical investigations, Sens. Actuators B 225 (2016) (2016) 463–468.

[74] V. Krishnakumar, R. Ramasamy, Scaled quantum chemical studies of the structure and vibrational spectra of 2-(methylthio) benzimidazole, Spectrochim. Acta Part A 62 (2005) 570–577.

[75] I. Milošev, H.-H. Strehblow, Electrochemical behaviour of Cu-*x*Zn alloys in borate buffer solution at pH 9.2, J. Electrochem. Soc. 150 (11) (2003) B517–B524.

[76] T. Kosec, D. Kek Merl, I. Milošev, Impedance and XPS study of benzotriazole films formed on copper, copper-zinc alloys and zinc in chloride solution, Corros. Sci. 50 (2008) 1987–1997.

[77] N. Sandhyarani, T. Pradeep, Ion/surface reactions at monolayer in solutions: a combined surface enhanced raman X-ray photoelectron spectroscopic investigation of the chemical modification of a 2-mercaptobenzothiazole monolayer on polycrystalline Au films, J. Colloid Interface Sci. 218 (1999) 176–183.

[78] T. Yoshida, K. Yamasaki, S. Sawada, An X-ray photoelectron spectroscopic study of 2-mercaptobenzothiazole metal complexes, Bull. Chem. Soc. Jpn. 52 (10) (1979) 2908–2912.

[79] B. Wrzosek, J. Bukowska, Molecular structure of 3-amino-5-mercapto-1,2,4-triazole self-assembled monolayers on Ag and Au surfaces, J. Phys. Chem. C 111 (2007) 17397–17403.

[80] N. Kovačević, A. Kokalj, DFT study of interaction of azoles with Cu(111) and Al (111) surfaces: role of azole nitrogen atoms and dipole–dipole interactions, J. Phys. Chem. C 115 (2011) 24189–24197, https://doi.org/10.1021/jp207076w.

[81] N. Kovačević, A. Kokalj, The relation between adsorption bonding and corrosion inhibition of azole molecules on copper, Corros. Sci. 73 (2013) 7–17, https://doi.org/10.1016/j.corsci.2013.03.016.

[82] D. Gustinčič, A. Kokalj, DFT Study of azole corrosion inhibitors on Cu_2O model of oxidized copper surfaces: I. molecule–surface and Cl–surface bonding, Metals 8 (2018) 310, https://doi.org/10.3390/met8050310.

[83] A. Kokalj, D. Gustinčič, M. Poberžnik, M. Lozinšek, New insights into adsorption bonding of imidazole: a viable C2–H bond cleavage on copper surfaces, Appl. Surf. Sci. 479 (2019) 463–468, https://doi.org/10.1016/j.apsusc.2018.12.246.

[84] M. Dlouhy, A. Kokalj, How adsorbed H, O, OH, and Cl affect plain adsorption of imidazole on copper, Corros. Sci. 205 (2022) 110443, https://doi.org/10.1016/j.corsci.2022.110443.

[85] A. Kokalj, M. Dlouhy, Dissociative adsorption of azoles on Cu(111) promoted by chemisorbed O and OH, Corros. Sci. 209 (2022) 110680, https://doi.org/10.1016/j.corsci.2022.110680.

[86] E. Vernack, D. Costa, P. Tingaut, P. Marcus, DFT studies of 2-mercaptobenzothiazole and 2-mercaptobenzimidazole as corrosion inhibitors for copper, Corros. Sci. 174 (2020) 108840, https://doi.org/10.1016/j.corsci.2020.108840.
[87] F. Chiter, D. Costa, V. Maurice, P. Marcus, Adsorption of 2-mercaptobenzimidazole corrosion inhibitor on copper: DFT study on model oxidized interfaces, J. Electrochem. Soc. 167 (2020) 161506, https://doi.org/10.1149/1945-7111/abcd4f.
[88] F. Chiter, D. Costa, V. Maurice, P. Marcus, Atomic scale insight into corrosion inhibition: DFT study of 2-mercaptobenzimidazole on locally de-passivated copper surfaces, J. Electrochem. Soc. 168 (2021) 121507, https://doi.org/10.1149/1945-7111/ac405c.
[89] S. Sun, Y. Geng, L. Tian, S. Chen, Y. Yan, S. Hu, Density functional theory study of imidazole, benzimidazole and 2-mercaptobenzimidazole adsorption onto clean Cu (111) surface, Corros. Sci. 63 (2012) 140–147, https://doi.org/10.1016/j.corsci.2012.05.024.
[90] A. El-Asri, A. Jmiai, H. Bourzi, Y. Lin, S. El Issami, Chemistry of the interaction between imidazole derivatives as corrosion inhibitors molecules and copper/brass/zinc surfaces: a DFT, reactive and classical molecular force fields study, Surf. Interfaces 44 (2024) 103799, https://doi.org/10.1016/j.surfin.2023.103799.
[91] X. Xu, A. Zuo, S. Liu, Y. Tang, DFT study on the adsorption of 1H-benzotriazole on the (1 1 1) surface of modelled Cu–25%Zn brass, Mater. Chem. Phys. 312 (2024) 128683, https://doi.org/10.1016/j.matchemphys.2023.128683.
[92] S. Peljhan, J. Koller, A. Kokalj, The effect of surface geometry of copper on adsorption of benzotriazole and Cl. Part I, J. Phys. Chem. C 118 (2014) 933–943, https://doi.org/10.1021/jp409717e.
[93] A. Kokalj, S. Peljhan, J. Koller, The effect of surface geometry of copper on dehydrogenation of benzotriazole. Part II, J. Phys. Chem. C 118 (2014) 944–954, https://doi.org/10.1021/jp409719c.
[94] A. Kokalj, E. Gregori, B. Kapun, I. Milošev, The Importance of Chemical Transformations of Adsorbed Molecules for Corrosion Inhibition: Mercaptobenzimidazoles on Copper, in preparation.
[95] Wikipedia. (2023). ⟨https://en.wikipedia.org/w/index.php?title=Elastic_properties_of_the_elements_(data_page)&oldid=1184786325⟩ . (Accessed 15 December 2023).